JOURNAL OF COMPUTATIONAL PHYSICS **145,** 193–227 (1998)
ARTICLE NO. CP985995

Marangoni–Bénard Convection with a Deformable Free Surface

K. A. Cliffe* and S. J. Tavener†

*A.E.A. Technology, Harwell Laboratory, Didcot, Oxfordshire OX11 0RA, United Kingdom; and †Department of Mathematics, The Pennsylvania State University, University Park, Pennsylvania 16802
E-mail: andrew.cliffe@aeat.co.uk and tavener@math.psu.edu

Received July 21, 1997; revised December 31, 1997

Computations of Marangoni convection are usually performed in two- or three-dimensional domains with rigid boundaries. In two dimensions, allowing the free surface to deform can result in a solution set with a qualitatively different bifurcation structure. We describe a finite-element technique for calculating bifurcations that arise due to thermal gradients in a two-dimensional domain with a deformable free surface. The fluid is assumed to be Newtonian, to conform to the Boussinesq approximation, and to have a surface tension that varies linearly with temperature. An orthogonal mapping from the physical domain to a reference domain is employed, which is determined as the solution to a pair of elliptic partial differential equations. The mapping equations and the equilibrium equations for the velocity, pressure, and temperature fields and their appropriate nonlinear boundary conditions are discretized using the finite-element method and solved simultaneously by Newton iteration. Contact angles other than 90 degrees are shown to disconnect the transcritical bifurcations to flows with an even number of cells in the expected manner. The loss of stability to single cell flows is associated with the breaking of a reflectional symmetry about the middle of the domain and therefore occurs at a pitchfork bifurcation point for contact angles both equal to, and less than, 90 degrees.

1. INTRODUCTION

We consider a Newtonian fluid in a two-dimensional container as shown in Fig. 1, which is heated from below along its lower surface Γ_B. The container is assumed to have adiabatic sidewalls Γ_L and Γ_R, and the upper surface of the fluid Γ_F is exposed to the atmosphere. When the free surface Γ_F is horizontal, a conducting solution exists for which the free surface is an isothermal surface. This conducting solution is stable for sufficiently small

0021-9991/98 $25.00

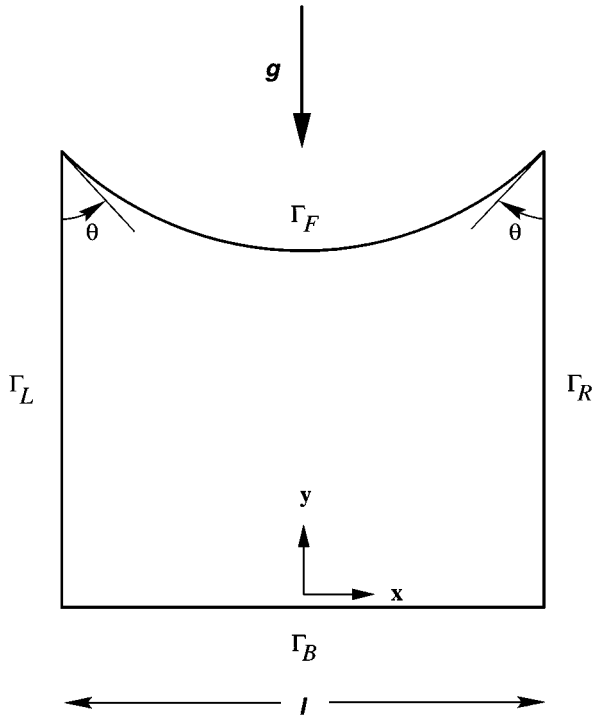

FIG. 1. Sketch of the physical domain.

temperature gradients, but loses stability to a convecting solution if the temperature of the bottom boundary is increased beyond a critical value. Pearson [1] has shown that for sufficiently thin layers the instability arises due to the temperature-dependent nature of the surface tension, rather than due to buoyancy effects. The instability due to an inverted density stratification dominates for thicker fluid layers.

For contact angles other than 90 degrees, the free surface is no longer an isothermal surface, and non-zero shear stresses exist along the free surface, arising due to the temperature-dependent nature of the surface tension. There is no conducting solution that satisfies both the equilibrium and boundary conditions. The effect of non-horizontal free surfaces on the qualitative nature of the bifurcation structure has previously been recognized by Davis [2]. His discussion concerns Marangoni convection in cylindrical geometries. On general grounds he argues that convecting $O(2)$-symmetric flows will arise continuously, but non-axisymmetric flows must develop at a symmetry-breaking bifurcation point. Analogous behaviour will be demonstrated for two-dimensional flows.

We investigate the effect of allowing contact angles other than 90 degrees and the attendant loss of a conducting solution. An orthogonal mapping technique described by Cliffe *et al.* [3] (and, for example, by Riskin and Leal [4]) is used to resolve the location of the deformable free surface. By seeking steady solutions only, we avoid the complex issues surrounding moving contact lines and time-dependent free surfaces. Since we can reasonably expect the free surface to be a (single-valued) function of the horizontal coordinate and we know a priori where the (steady) free surface is likely to be steepest, we are able to use a relatively simple mapping technique compared to the sophisticated methods described by Tsiveriotis and Brown [5] and Christadoulou and Scriven [6].

Nonlinearities are present in both the governing equations which pertain in the interior of the computational domain, and in the boundary conditions at the free surface. A jump in pressure exists across the free surface that is proportional to the product of the surface curvature and the (temperature-dependent) surface tension. We solve the full nonlinear problem, and make no assumptions regarding the relative sizes of the inertial and diffusive terms in the momentum equation. The contact angle need not be close to 90 degrees, nor need the free surface curvature be small.

By combining extended system methods for locating singular points (for implementation details see Cliffe *et al.* [7–9]) with the orthogonal mapping technique, we are able to investigate the roles of buoyancy, surface tension, and contact angle on the bifurcation structure of the solution set in a finite domain, when the free surface is required to be other than horizontal. In order to describe the disconnections that occur when the free surface is no longer constrained to be horizontal, we concentrate on flows for which the free-surface deformations are small. We do so, not because of any limitations of our method, but because, even for small free surface deformations, these disconnections become so large that it is difficult to observe the relationships that necessarily exist between the horizontal and non-horizontal free surface cases. The large quantitative effect of contact angles other than 90 degrees is illustrated in Fig. 6.

An essential component of our study was the use of a computer algebra system, in our case REDUCE [10]. A finite-element analysis of the coupled system of partial differential equations and boundary conditions governing the flow produces a finite-dimensional system of algebraic equations. First- and second-order derivatives of these equations were required in order to find regular solutions using Newton's method and to locate singular points, which were found as regular solutions of "extended systems" of equations. Derivatives with respect to both the variables and parameters were necessary in order to perform continuation with respect to a chosen parameter. The system of equations includes those describing the orthogonal mapping, and the variables include the coordinates of the physical domain. Automatic generation of the subroutines to compute derivatives was deemed to be essential. Quadratic convergence of the Newton iteration was observed in all cases. More sophisticated systems of elliptic equations to determine the mapping would make the use of a computer algebra system even more important.

Considerable success has already been achieved in computing the onset of Marangoni convection in non-deforming domains. Winters *et al.* [11], Dijkstra [12], Bergeon *et al.* [13], and Evrenselamet *et al.* [14] have examined flows in two-dimensional rectangular containers; Zaman and Narayanan [15] have considered the instability in cylindrical containers; and more recently, Dijkstra [16, 17] and Dauby and Lebon [18] have performed computations in three-dimensional domains. Other authors, amongst them Chen *et al.* [19], Floryan and Chen [20], Lu [21], Sasmal and Hochstein [22], and Chippada *et al.* [23] have performed computations of flows driven by thermocapillary forces in deformable domains, but they have all concentrated on the sidewall, rather than the bottom heated case. To the best of our knowledge the present study is the first application of extended system techniques to compute codimension-zero singularities (limit points and symmetry-breaking bifurcation points) of a deforming free surface flow.

Much of the interest in Marangoni convection has arisen in the context of microgravity environments due to the potential for growing high quality crystals in space. Kamotami *et al.* [24] show that in low gravity environments, surface deformations can be large and have a considerable affect on the flow. Kamotami and Platt [25] have addressed the simpler

computational problem of flows in curved, but fixed free surfaces. We also concentrate on the zero gravity case, but our technique assumes no surface location a priori, and permits the free surface to deform as necessary. Note for example, the asymmetry in the heights of the free surface at the left-hand and right-hand walls in Fig. 12, which was determined as part of the solution.

2. THE GOVERNING EQUATIONS

We consider the flow of a Newtonian fluid in a two-dimensional domain Ω with boundary Γ comprised of four parts $\Gamma_L, \Gamma_R, \Gamma_B$, and Γ_F, as sketched in Fig. 1. Letting the superscript * denote dimensional quantities and invoking the Boussinesq approximation, the continuity, momentum, and temperature equations are

$$\begin{aligned} \nabla_* \cdot \boldsymbol{u}^* &= 0, \\ \rho_0 \frac{D\boldsymbol{u}^*}{Dt^*} &= \nabla_* \cdot \tau^* - \rho g \boldsymbol{j}, \\ \frac{DT^*}{Dt^*} &= \kappa \nabla_*^2 T^*, \end{aligned} \tag{1}$$

where $\boldsymbol{u}^*(\boldsymbol{x}^*)$ is the velocity vector at position $\boldsymbol{x}^* \in \Omega$, $T^*(\boldsymbol{x}^*)$ is the temperature, and

$$\begin{aligned} \nabla_* &= \boldsymbol{i}\frac{\partial}{\partial x^*} + \boldsymbol{j}\frac{\partial}{\partial y^*}, \\ \nabla_*^2 &= \frac{\partial^2}{\partial x^{*2}} + \frac{\partial^2}{\partial y^{*2}}, \end{aligned}$$

where $\boldsymbol{i}$ and $\boldsymbol{j}$ are unit vectors in the x- and y-directions, respectively. The stress tensor τ^* is given by

$$\tau_{ij}^* = -p^* \delta_{ij} + \mu(u_{i,j}^* + u_{j,i}^*), \tag{2}$$

where $p^*(\boldsymbol{x}^*)$ is the pressure, μ is the molecular viscosity, and

$$u_{i,j}^* = \frac{\partial u_i^*}{\partial x_j^*}.$$

The fluid density $\rho(\boldsymbol{x}^*)$ is assumed to vary with temperature as

$$\rho(\boldsymbol{x}^*) = \rho_0[1 - \alpha(T^*(\boldsymbol{x}^*) - T_0)],$$

where T_0 is the temperature at the free surface of the conducting solution, ρ_0 is the density at temperature T_0, and α is the coefficient of thermal expansion. Consistent with the Boussinesq approximation, the temperature-dependent density ρ appears only in the gravitational body force term, where g is the acceleration due to gravity. Finally κ is the coefficient of thermal diffusion.

Equations (1) must be solved subject to the following boundary conditions,

$$
\begin{aligned}
\boldsymbol{u}^*(\boldsymbol{x}^*) &= \boldsymbol{0} && \text{for } \boldsymbol{x}^* \in \Gamma_L, \Gamma_B, \Gamma_R, \\
\boldsymbol{u}^* \cdot \boldsymbol{n} &= 0 && \text{for } \boldsymbol{x}^* \in \Gamma_F, \\
n_i \tau_{ij}^* n_j &= K^* \sigma(\boldsymbol{x}^*) && \\
&= K^*[\sigma_0 - \sigma_1(T^*(\boldsymbol{x}^*) - T_0)] && \text{for } \boldsymbol{x}^* \in \Gamma_F, \\
t_i \tau_{ij}^* n_j &= \boldsymbol{t} \cdot \nabla_* \sigma(\boldsymbol{x}^*) && \\
&= -\sigma_1[\boldsymbol{t} \cdot \nabla_* T^*(\boldsymbol{x}^*)] && \text{for } \boldsymbol{x}^* \in \Gamma_F, \\
T^*(\boldsymbol{x}^*) &= T_1 && \text{for } \boldsymbol{x}^* \in \Gamma_B, \\
\boldsymbol{n} \cdot \nabla_* T^*(\boldsymbol{x}^*) &= 0 && \text{for } \boldsymbol{x}^* \in \Gamma_L, \Gamma_R, \\
-k_0[\boldsymbol{n} \cdot \nabla_* T^*(\boldsymbol{x}^*)] &= h(T^*(\boldsymbol{x}^*) - T_0) && \text{for } \boldsymbol{x}^* \in \Gamma_F,
\end{aligned}
\tag{3}
$$

where $\boldsymbol{n}$ and $\boldsymbol{t}$ are respectively the outward normal and tangent vectors on Γ, and K^* is the curvature of the free surface. The surface tension σ is assumed to vary linearly with temperature as

$$
\sigma(\boldsymbol{x}^*) = \sigma_0 - \sigma_1(T^*(\boldsymbol{x}^*) - T_0), \qquad \text{for } \boldsymbol{x}^* \in \Gamma_F,
$$

where σ_0 is the surface tension at temperature T_0 and σ_1 is the rate of change of surface tension with temperature. In the boundary condition for the temperature field at the free surface, k_0 is the thermal conductivity of the fluid and h is the surface thermal conductance.

We non-dimensionalize Eqs. (1) and boundary conditions (3) by choosing appropriate length, velocity, and temperature scales. The depth of an undeformed fluid layer of equal volume is chosen as the length scale d, i.e., $d = \text{volume}/l$, where l is the length of the domain. The "Marangoni" velocity $V_M = (\sigma_1 \beta d)/\mu$ is chosen as the velocity scale, where β is the average temperature gradient from bottom to top. The appropriate time scale is then $d/V_M = \mu/(\sigma_1 \beta)$. Temperatures are non-dimensionalized as $T = (T^* - T_0)/(\beta d)$. We define seven non-dimensional quantities,

$$
\begin{aligned}
&\text{Aspect ratio,} && \eta = \frac{l}{d}, \\
&\text{Biot number,} && L = \frac{hd}{k_0}, \\
&\text{Bond number,} && G = \frac{\rho_0 g d^2}{\sigma_0}, \\
&\text{Capillary number,} && Ca = \frac{\mu\kappa}{\sigma_0 d}, \\
&\text{Marangoni number,} && M = \frac{\sigma_1 \beta d^2}{\mu\kappa}, \\
&\text{Prandtl number,} && Pr = \frac{\mu}{\rho_0 \kappa}, \\
&\text{Rayleigh number,} && R = \frac{\rho_0 \alpha \beta g d^4}{\mu\kappa},
\end{aligned}
\tag{4}
$$

so that Eqs. (1) become

$$\begin{aligned} \nabla \cdot \boldsymbol{u} &= 0, \\ \frac{M}{Pr}\frac{D\boldsymbol{u}}{Dt} &= \nabla \cdot \tau + \left(\frac{RT}{M} - \frac{G}{MC}\right)\boldsymbol{j}, \\ M\frac{DT}{Dt} &= \nabla^2 T, \end{aligned} \tag{5}$$

where

$$\begin{aligned} \nabla &= \boldsymbol{i}\frac{\partial}{\partial x} + \boldsymbol{j}\frac{\partial}{\partial y}, \\ \nabla^2 &= \frac{\partial^2}{\partial x^2} + \frac{\partial^2}{\partial y^2}, \\ \tau_{ij} &= -p\delta_{ij} + (u_{i,j} + u_{j,i}), \end{aligned} \tag{6}$$

and $\tau = \tau^*/(\sigma_1\beta)$ and $p = p^*/(\sigma_1\beta)$.

The boundary conditions (3) become

$$\begin{aligned} \boldsymbol{u} &= \boldsymbol{0} && \text{for } \boldsymbol{x} \in \Gamma_L, \Gamma_B, \Gamma_R, \\ \boldsymbol{u} \cdot \boldsymbol{n} &= 0 && \text{for } \boldsymbol{x} \in \Gamma_F, \\ n_i \tau_{ij} n_j &= K\left(\frac{1}{MC} - T\right) && \text{for } \boldsymbol{x} \in \Gamma_F, \\ t_i \tau_{ij} n_j &= -\boldsymbol{t} \cdot \nabla T && \text{for } \boldsymbol{x} \in \Gamma_F, \\ T &= 2 && \text{for } \boldsymbol{x} \in \Gamma_B, \\ \boldsymbol{n} \cdot \nabla T &= 0 && \text{for } \boldsymbol{x} \in \Gamma_L, \Gamma_R, \\ \boldsymbol{n} \cdot \nabla T + LT &= 0 && \text{for } \boldsymbol{x} \in \Gamma_F, \end{aligned} \tag{7}$$

where $K = K^* d$.

Noting that

$$\boldsymbol{u} \cdot \boldsymbol{n} = 0 \qquad \text{on } \Gamma,$$

we recognize that one of the (local) element divergence constraints is redundant, and it is replaced by a global volume constraint.

3. ORTHOGONAL MAPPING TECHNIQUE

In this section we briefly review the orthogonal mapping technique for solving viscous free-surface flows that has been previously described by Cliffe *et al.* [3]. Cliffe *et al.* used this approach to compute the free surface location of laminar flows down a shallow inclined plane and over two sinusoidal bumps. Their results were compared with laboratory measurements of the free surface heights for a range of Reynolds numbers varying from 0.3 to 25. For all flow rates, the computations and experiments were found to agree to within 2% in an appropriate norm.

Let $\Omega(x, y)$ be the physical domain with four sides Γ_L, Γ_B, Γ_R, and Γ_F such as shown in Fig. 1. We construct an orthogonal mapping $(\psi(x, y), \phi(x, y))$ from Ω onto a reference domain Ω' where

$$\Omega' = \left\{(\psi, \phi) : (\psi, \phi) \in \left[-\tfrac{1}{2}, \tfrac{1}{2}\right] \times [0, 1]\right\}, \tag{8}$$

such that the level curves of $\psi(x, y)$ and $\phi(x, y)$ are orthogonal, and the boundaries Γ_L, Γ_B, Γ_R, and Γ_F are mapped onto $\psi = -\frac{1}{2}$, $\phi = 0$, $\psi = \frac{1}{2}$, and $\phi = 1$, respectively. The system of partial differential equations and boundary conditions governing the flow in the physical domain $\Omega(x, y)$ is then recast in terms of the new independent variables $(\psi, \phi) \in \Omega'$. The partial differential equations and boundary conditions defining the orthogonal transformation are added to the equations governing the flow, and the combined system is solved using a conventional finite-element approach. The resulting nonlinear system of algebraic equations is solved by Newton's method.

The coordinate transformation is orthogonal if

$$\nabla\psi \cdot \nabla\phi = 0 \qquad \text{for all } (x, y) \in \Omega,$$

which has the general solution

$$\begin{aligned} \psi_x &= \lambda\phi_y, \\ \psi_y &= -\lambda\phi_x, \end{aligned} \tag{9}$$

where λ depends on (x, y) (or equivalently (ψ, ϕ)). Using

$$\psi_x = J^{-1}y_\phi, \qquad \psi_y = -J^{-1}x_\phi, \qquad \phi_x = -J^{-1}y_\psi, \qquad \phi_y = J^{-1}x_\psi,$$

where

$$J = \frac{\partial(x, y)}{\partial(\psi, \phi)} = \det\begin{pmatrix} x_\psi & x_\phi \\ y_\psi & y_\phi \end{pmatrix}$$

is the Jacobian of the transformation, Eqs. (9) become

$$\begin{aligned} y_\phi &= \lambda x_\psi, \\ x_\phi &= -\lambda y_\psi. \end{aligned} \tag{10}$$

Assuming $x(\psi, \phi)$ and $y(\psi, \phi)$ to have continuous second derivatives, equating cross derivatives of $y(\psi, \phi)$ and $x(\psi, \phi)$ respectively from (10), we have

$$\left(\frac{x_\phi}{\lambda}\right)_\phi + (\lambda x_\psi)_\psi = 0, \tag{11}$$

$$\left(\frac{y_\phi}{\lambda}\right)_\phi + (\lambda y_\psi)_\psi = 0, \tag{12}$$

which, given $\lambda(\psi, \phi)$, provide two elliptic partial differential equations for (x, y) on Ω'.

The boundary conditions for $x(\psi, \phi)$ and $y(\psi, \phi)$ are derived from the shapes of the fixed boundaries of the physical domain Ω, from the orthogonality condition along the boundaries of Ω, from the kinematic boundary condition along the free surface Γ_F, and from the required contact angles. They are

$$\begin{aligned} x = -\eta/2, \qquad & y_\psi = 0 \qquad && \text{on } \psi = -\frac{1}{2}, \\ x_\phi = 0, \qquad & y = 0 \qquad && \text{on } \phi = 0, \\ x = \eta/2, \qquad & y_\psi = 0 \qquad && \text{on } \psi = \frac{1}{2}, \\ \lambda^{-1} x_\phi = -y_\psi \qquad & -u y_\psi + v x_\psi = 0 \qquad && \text{on } \phi = 1, \\ & x_\psi + y_\psi \tan\theta = 0 \qquad && \text{at } (\psi, \phi) = \left(-\tfrac{1}{2}, 1\right), \\ & x_\psi - y_\psi \tan\theta = 0 \qquad && \text{at } (\psi, \phi) = \left(\tfrac{1}{2}, 1\right), \end{aligned} \tag{13}$$

where η is the aspect ratio defined in Section 2, and θ is the prescribed contact angle.

For simplicity, we shall require that $\lambda(\psi, \phi)$ be constant in Ω' and achieve this by solving

$$\nabla_{\prime}^2 \lambda(\psi, \phi) = 0, \tag{14}$$

with boundary conditions

$$\boldsymbol{n}' \cdot \nabla_{\prime} \lambda = 0 \qquad \text{for all } (\psi, \phi) \in \Gamma', \tag{15}$$

where

$$\nabla_{\prime} = \boldsymbol{i} \frac{\partial}{\partial \psi} + \boldsymbol{j} \frac{\partial}{\partial \phi},$$

$$\nabla_{\prime}^2 = \frac{\partial^2}{\partial \psi^2} + \frac{\partial^2}{\partial \phi^2},$$

and $\boldsymbol{n}'$ is the outward-directed normal on the boundary Γ'. The constant value of λ is determined by invoking the orthogonality conditions at an interior point of Ω', e.g.,

$$y_\phi + x_\phi = \lambda(x_\psi - y_\psi) \qquad \text{at } (\psi, \phi) = \left(0, \tfrac{1}{2}\right). \tag{16}$$

The corresponding weak equations are developed in Appendix A.

4. LOCATING SINGULARITIES

4.1. *Computation of Z_2 Symmetry-Breaking Points*

The weak equations presented in Appendix A were solved via the finite-element method using isoparametric quadrilateral elements with biquadratic interpolation of the physical coordinates x and y, the velocity components u and v, and the temperature T. Discontinuous linear interpolation of the pressure field was employed. The resulting nonlinear system of

equations may be written as

$$\boldsymbol{f}(\boldsymbol{a}, \boldsymbol{b}) = \boldsymbol{0}, \qquad \boldsymbol{f} : R^N \times R^p \mapsto R^N. \tag{17}$$

The finite-dimensional system of nonlinear algebraic equations (17) is equivariant with respect to an $(N \times N)$ orthogonal matrix S, such that $S^2 = I$, but $S \neq I$, i.e.,

$$S\boldsymbol{f}(\boldsymbol{a}, \boldsymbol{b}) = \boldsymbol{f}(S\boldsymbol{a}, \boldsymbol{b}). \tag{18}$$

The orthogonal matrix S induces a unique decomposition of R^N into symmetric and anti-symmetric subspaces,

$$R^N = R_s^N \oplus R_a^N,$$

where

$$R_s^N = \{\boldsymbol{x} \in R^N : S\boldsymbol{a} = \boldsymbol{a}\},$$
$$R_a^N = \{\boldsymbol{x} \in R^N : S\boldsymbol{a} = -\boldsymbol{a}\}.$$

Symmetric solutions are those for which

$$\begin{aligned} x(\psi, \phi) &= -x(-\psi, \phi), \\ y(\psi, \phi) &= y(-\psi, \phi), \\ \lambda(\psi, \phi) &= \lambda(-\psi, \phi), \\ u(\psi, \phi) &= -u(-\psi, \phi), \\ v(\psi, \phi) &= v(-\psi, \phi), \\ p(\psi, \phi) &= p(-\psi, \phi), \\ T(\psi, \phi) &= T(-\psi, \phi). \end{aligned}$$

Anti-symmetric solutions are those for which

$$\begin{aligned} x(\psi, \phi) &= x(-\psi, \phi), \\ y(\psi, \phi) &= -y(-\psi, \phi), \\ \lambda(\psi, \phi) &= -\lambda(-\psi, \phi), \\ u(\psi, \phi) &= u(-\psi, \phi), \\ v(\psi, \phi) &= -v(-\psi, \phi), \\ p(\psi, \phi) &= -p(-\psi, \phi), \\ T(\psi, \phi) &= -T(-\psi, \phi). \end{aligned}$$

At a symmetry breaking bifurcation point $(\boldsymbol{a}_0, \boldsymbol{b}_0)$,

$$\left.\frac{\partial \boldsymbol{f}}{\partial \boldsymbol{a}}\right|_{(\boldsymbol{a}_0, \boldsymbol{b}_0)} \boldsymbol{z} = \boldsymbol{0},$$

where $\boldsymbol{a}_0 \in R_s^N$ and the null eigenvector, $\boldsymbol{z} \in R_a^N$.

Since the symmetries of the solution and eigenvector are known, all computations may be performed in one-half of the domain. The boundary conditions appropriate to Ω'_- where

$$\Omega'_- = \left\{(\psi,\phi) : (\psi,\phi) \in \left[-\tfrac{1}{2}, 0\right] \times [0,1]\right\}$$

are

$$x_\phi = 0, \qquad y = 0, \qquad u = v = 0, \qquad T = 2 \quad \text{for } \psi \in \left[-\tfrac{1}{2}, 0\right], \phi = 0,$$

$$x = -\eta/2, \qquad y_\psi = 0, \qquad u = v = 0, \qquad T_\psi = 0 \quad \text{for } \psi = -\frac{1}{2}, \phi \in [0,1],$$

$$x_\psi + y_\psi \tan\theta = 0 \qquad \text{at } (\psi,\phi) = \left(-\tfrac{1}{2}, 1\right),$$

$$\int_{\psi=-1/2}^{\psi=0} -y_\psi \, d\psi = 0 \qquad \text{for } \phi = 1,$$

$$-uy_\psi + vx_\psi = 0 \qquad \text{for } \psi \in \left[-\tfrac{1}{2}, 0\right], \quad \phi = 1,$$

$$\int_{\psi=-1/2}^{\psi=0} \left(\frac{1}{MC} - T\right) x_\psi \frac{1}{\sqrt{x_\psi^2 + y_\psi^2}} \, d\psi = 0 \qquad \text{for } \phi = 1,$$

$$\int_{\psi=-1/2}^{\psi=0} \left(\frac{1}{MC} - T\right) y_\psi \frac{1}{\sqrt{x_\psi^2 + y_\psi^2}} \, d\psi = 0 \qquad \text{for } \phi = 1, \tag{19}$$

$$\int_{\psi=-1/2}^{\psi=0} LT\sqrt{x_\psi^2 + y_\psi^2} \, d\psi = 0 \qquad \text{for } \phi = 1.$$

Odd symmetry boundary conditions on x for $\psi = 0, \phi \in [0,1]$.
Even symmetry boundary conditions on y for $\psi = 0, \phi \in (0,1)$.
Even symmetry boundary conditions on λ for $\psi = 0, \phi \in [0, \frac{1}{2}) \cup (\frac{1}{2}, 1]$,
and $y_\phi + x_\phi = \lambda(x_\psi - y_\psi)$ at $(\psi,\phi) = (0, \frac{1}{2})$.
Odd symmetry boundary conditions on u for $\psi = 0, \phi \in (0,1]$.
Even symmetry boundary conditions on v, T for $\psi = 0, \phi \in (0,1]$.

When computing a symmetric solution on Ω'_-, a global volume condition is required. Non-slip velocity boundary conditions are imposed along $\phi = 0$ and $\psi = -\frac{1}{2}$, the kinematic condition is applied along the free surface $\phi = 1$, and $u = 0$ along the symmetry axis $\psi = 0$ by symmetry. In other words

$$\mathbf{u} \cdot \mathbf{n} = 0 \qquad \text{on } \Gamma,$$

and one of the (local) element divergence constraints is redundant. We replace one of the element divergence constraints by a global volume constraint. When computing the null eigenvector on one-half of the domain, the u-velocity component of the eigenvector $\hat{u}$ is not required to vanish by symmetry along $\psi = 0$. All element divergence constraints are required and we remove the global constraint and retain all the pressure equations when computing the null eigenvector.

The λ components of the null eigenvector $\hat{\lambda}$ are required to be zero everywhere. In order to ensure this we replace the orthogonality condition on λ at $(0, \frac{1}{2})$ used when computing the solution with a condition that $\hat{\lambda} = 0$ at $(0, \frac{1}{2})$ when computing the eigenvector.

At a singular point, the kinematic condition requires that

$$-u\frac{\partial \hat{y}}{\partial \psi} + v\frac{\partial \hat{x}}{\partial \psi} - \hat{u}\frac{\partial y}{\partial \psi} + \hat{v}\frac{\partial x}{\partial \psi} = 0, \tag{20}$$

along the free surface, where u and v are the two velocity components of the solution and $\hat{u}$ and $\hat{v}$ denote the two velocity components of the null eigenvector. Equation (20) is used to determine the y-component of the null eigenvector $\hat{y}$ at each node along the free surface. For all symmetric solutions, regardless of the value of the contact angle, the velocity components u and v are zero at the centre of the free surface. Both $u = 0$ and $\frac{\partial y}{\partial \psi} = 0$ by symmetry. The latter condition requires that the free surface has zero slope at the centerline and therefore $v = 0$ at the centerline. Along the symmetry axis, Eq. (20) reduces to $\hat{v} = 0$, since $\frac{\partial x}{\partial \psi} \neq 0$ along $\psi = 0$. For symmetric solutions, the v-component of velocity is symmetric about $\psi = 0$, so the v-component of a symmetry-breaking eigenvector must be antisymmetric about $\psi = 0$, and therefore $\hat{v}$ must be zero along the symmetry axis. We see that the kinematic condition used to determine $\hat{y}$ at the middle of the free surface is identical to the condition on $\hat{v}$ which is imposed by symmetry. A naive implementation will have two linearly dependent equations. A non-singular system of equations is obtained by replacing (20) at $\psi = 0$ with $\hat{y} = 0$, since the y-component of the eigenvector must be zero along $\psi = 0$ by reason of it being antisymmetric about $\psi = 0$.

With these extra conditions, the Werner–Spence extended system [26] can be used as usual.

4.2. *Computation of Limit Points*

When computing limit points along branches of symmetric solutions, at which the null eigenvector is symmetric, the problems described in the previous section do not arise, since there is no symmetry requirement for $\hat{v}$ to be zero along the centerline. Indeed in the interior of the flow, the v-component of the eigenvector is non-zero along $\psi = 0$ and is required to be zero at the free surface due to the kinematic boundary condition only. (For symmetric solutions, the free surface must be horizontal at the centerline and $u = 0$ along the centerline.) When computing on Ω'_-, we retain the global constraint when computing the eigenvector, since for symmetric eigenvectors

$$\hat{\mathbf{u}} \cdot \mathbf{n} = 0 \qquad \text{on } \Gamma.$$

We again force $\hat{\lambda}$ to be zero at $(0, \frac{1}{2})$. With this provision, the Moore–Spence extended system [27] may then be used directly.

5. RESULTS

Our particular implementation of the orthogonal mapping technique has been successfully tested against laboratory measurements of the free-surface flow down an inclined plane and over two sinusoidal bumps for a range of flow rates as reported in Cliffe *et al*. [3].

An additional test problem was investigated in order to determine convergence behaviour. In the absence of gravity and temperature gradients, there is no fluid motion in a two-dimensional domain like that shown in Fig. 1, and the free surface has constant curvature and is an arc of a circle whose radius is dependent upon the contact angle. This is one of the

few exact solutions of the Navier–Stokes equations with a non-horizontal free surface, if unfortunately a very simple one. However, since the arc of a circle cannot be represented exactly using piecewise quadratic interpolation of the mapping functions $x(\psi, \phi)$ and $y(\psi, \phi)$, we can use this exact solution to study the rate of convergence of our method. Due to the normal stress boundary condition, the location of the free surface depends on the curvature of the surface and thereby on second derivatives of $x(\psi, \phi)$ and $y(\psi, \phi)$. These variables are interpolated by piecewise quadratic functions on quadrilateral elements. Girault and Raviart [28, p. 158] show that the *global* convergence of the interpolant is cubic in the L_2 semi-norm and quadratic in the H^1 semi-norm. Their result cannot be extended to the H^2 semi-norm since this is undefined (even weakly) for the interpolant. We consider instead the interpolation on an element-by-element basis. Brenner and Scott [29, p. 104] show that on each element the local interpolant converges linearly in h in the H^2 semi-norm. By summing over all elements [29, p. 107] they then obtain an appropriate equivalent global estimate. The linear convergence of the free surface location observed in Table 1 reflects the linear convergence of the interpolant in the H^2 semi-norm. The pressure field converges linearly to a constant pressure field that is equal to the product of the surface tension and surface curvature. Since we would expect a piecewise linear interpolant to represent a constant field exactly on any mesh, the observed linear convergence of the pressure field is a further consequence of the linear convergence of the free surface. If, by contrast, the nodes along the free surface are *constrained* to lie on the arc of a circle, and the normal and tangential stress boundary conditions along the curved surface are used to solve for the two velocity components, the solution to the discrete equations reproduces the exact (constant) pressure field on any mesh.

As a third test, we considered the onset of convection in the absence of gravity with a 90-degree contact angle. In Table 2 we show the effect of decreasing capillary number on the location of three different critical points. The first critical Marangoni number Ma_{B1} indicates the loss of stability of the conducting solution at a symmetry-breaking bifurcation to a single-cell flow at an aspect ratio of one. The second critical Marangoni number Ma_{T1} indicates the loss of stability of the conducting solution at a transcritical bifurcation point to a two-cell flow at an aspect ratio of two. The Marangoni numbers in the final column, Ma_{L_1}, are those at the limit point associated with the transcritical bifurcation to two-cell flows at an aspect ratio of two. For this test, the other parameters were Rayleigh number zero, Bond number zero, Biot number one, and Prandtl number one. The corresponding critical Marangoni numbers computed by Winters *et al.* [11] on equivalent meshes with a horizontal, non-deforming upper surface, complete the table. As expected, the critical

TABLE 1
Convergence Study in the Absence of Gravity and Temperature Gradients

Mesh	L_2 velocity error	L_2 pressure error	L_2 surface error
2×2	0.1833E+00	0.2107E+00	0.8037E−02
4×4	0.1242E−01	0.2186E−01	0.5173E−03
8×8	0.2547E−02	0.4839E−01	0.7405E−03
16×16	0.2757E−03	0.3495E−01	0.3543E−03
32×32	0.2806E−04	0.2267E−01	0.1567E−03
64×64	0.2883E−05	0.1451E−01	0.6881E−04

TABLE 2
Comparison of Critical Marangoni Numbers for Deforming and Rigid Upper Surfaces

Ca	Ma_{B1}	Ma_{T1}	Ma_{L1}
5.0E−03	140.18	137.23	137.20
4.0E−03	159.38	147.58	147.48
3.0E−03	178.42	154.96	154.80
2.0E−03	193.98	159.83	159.63
1.0E−03	205.03	163.07	162.85
1.0E−04	211.61	165.11	164.88
1.0E−05	212.14	165.29	165.06
rigid[11]	212.27	165.307	165.119

Marangoni numbers approach those on an undeforming domain as the surface tension at T_0, i.e., σ_0, increases. The two bifurcation points reported in [11] lie on the convecting solution branch for which the velocity field is identically zero and the temperature field is linear with isotherms that are parallel to the free surface.

Contact angles other than 90 degrees produce a qualitative change in the nature of the solution set. When the contact angle is 90 degrees, a conducting solution exists for which the free surface is an isothermal surface. If the free surface is forced to be concave or convex because the contact angle is greater than or less than 90 degrees, the free surface cannot be an isothermal surface and unbalanced surface tension forces must act along it. These unbalanced forces necessarily drive a flow whose strength depends upon the Marangoni number. As a result of the loss of a conducting or "trivial" solution, the transcritical bifurcation to two-cell flows is disconnected.

If the free surface is concave, the primary branch, i.e., the solution branch that is continuously connected to the unique solution at small Marangoni number, is a two-cell flow with upwelling along the centreline. Two-cell flows with down-welling along the centreline occur as disconnected solutions. It is reasonable that two-cell flows with upwelling along the centreline should be preferred, since the concave free surface is hotter at its middle (which is nearer the hot bottom surface) than at its sides. Unbalanced surface tension forces are therefore directed from the centre towards the wall.

The loss of stability to single-cell flows is associated with the breaking of the Z_2 symmetry about the vertical midplane. Provided the contact angles at the left-hand and right-hand walls are equal, solutions along the primary solution branch respect this symmetry, and single-cell flows still arise at a pitchfork bifurcation point.

All the computations discussed below were performed with Rayleigh number zero, Bond number zero, Biot number one, and Prandtl number one. Loci of singular points for a contact angle of 89.4 degrees and capillary number of 10^{-5} are shown in Fig. 2. A contact angle near

FIG. 2. Loci of singular points for $\theta = 89.43$ degrees and $Ca = 10^{-5}$. The solid curve *ACB* is a locus of symmetry-breaking bifurcation points on the primary two-cell branch, and the chained line *HQ*, is a locus of limit points on the one-cell branches. The solid curve *DE*, is a locus of limit points on the disconnected two-cell branch, and the dashed line *FG*, is a locus of symmetry-breaking bifurcation points on this branch. The narrow dashed lines are paths of bifurcation points for $\theta = 90$ degrees and $Ca = 10^{-5}$. (a) Detail near quartic point Q. (b) Detail near double singular point M.

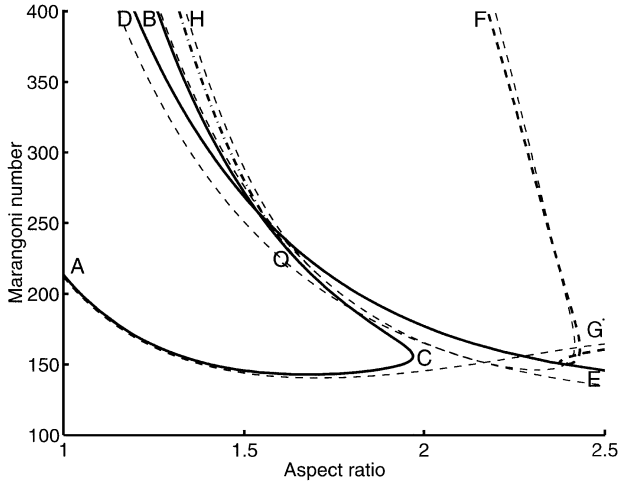
D
B
H
F
A
Q
C
G
E
Marangoni number
Aspect ratio
400
350
300
250
200
150
100
1
1.5
2
2.5

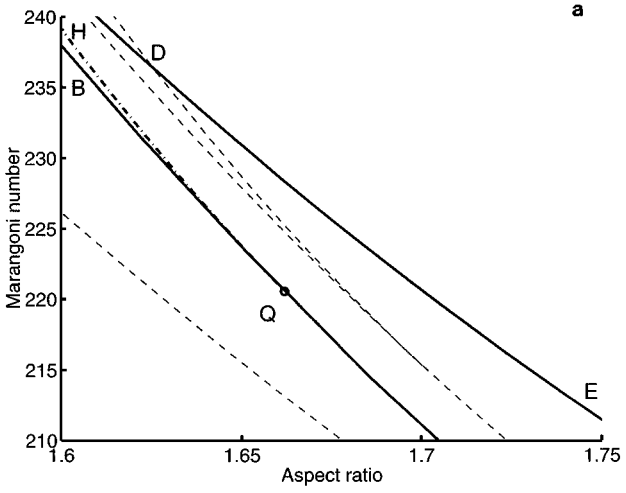
a
H
D
B
Q
E
Marangoni number
Aspect ratio
240
235
230
225
220
215
210
1.6
1.65
1.7
1.75

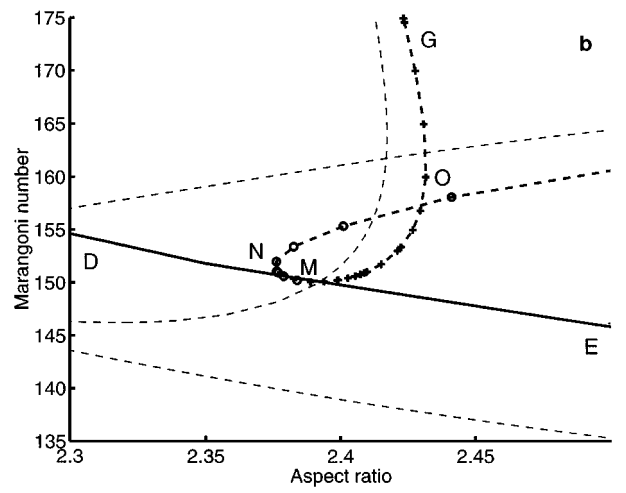
b
G
O
N
M
D
E
Marangoni number
Aspect ratio
175
170
165
160
155
150
145
140
135
2.3
2.35
2.4
2.45

90 degrees and a small capillary number were chosen so as to highlight the connections with the known results for a rigid horizontal free surface, not because of any inherent limitations in our method. The solid curve *ACB* is a path of symmetry-breaking bifurcation points on the primary solution branch. The primary branch is the branch of solutions that is continuously connected to the unique solution at small Marangoni numbers. Solutions along the primary branch are two-cell flows with upwelling along the centreline. The point C is a $C+$ coalescence point (see [9]) from which a closed loop of one-cell flows develops. The chained line, *HQ*, is a path of limit points along the one-cell flow branches. It terminates at a quartic bifurcation point Q, where the bifurcation to single cell flows has locally quartic contact. The quartic point Q indicates the aspect ratio at which the symmetry-breaking bifurcation at the larger Marangoni number along the primary branch changes from supercritical to subcritical. For aspect ratios less than that at the quartic bifurcation point, the one-cell flows will demonstrate hysteresis.

The other solid curve *DE* in Fig. 2 is the locus of limit points along the disconnected two-cell branch. Two-cell flows with down-welling along the centreline exist for Marangoni numbers exceeding that along *DE*. These two-cell flows are, however, unstable with respect to anti-symmetric disturbances until the Marangoni number exceeds that along a locus of secondary bifurcation points, a part of which is indicated by the dashed line *FG*.

The thin dashed lines in Fig. 2 represent loci of singularities for the case with 90 degree contact angles and capillary number of 10^{-5}. The critical Marangoni numbers for the bifurcations to one- and two-cell flows are shown, as are the critical Marangoni numbers at turning points along the one-cell solution branches and at secondary (symmetry-breaking) bifurcation points along the two-cell solution branches.

Details near the quartic point Q and a double singular point M are shown in Figs. 2a and 2b, respectively. The apparent self intersection of the path of symmetry-breaking bifurcation points in Fig. 2b is avoided as these bifurcations lie on two different solution surfaces. Secondary bifurcation points that lie on the disconnected branch of two-cell solutions (with downwelling along the centreline) are indicated by $+$. Secondary bifurcation points that lie on the solution branch corresponding to the conducting solution for horizontal free surfaces, are indicated by $\circ$. The point M is a double singular point, where the turning point along the disconnected branch of two-cell flows and a symmetry-breaking bifurcation point are coincident. A $C+$ coalescence point N, and a $C-$ coalescence point O, are also present in this figure.

In Figs. 3, 4, and 5 we plot the computed bifurcation diagrams at aspect ratios 1.6, 1.7, and 2.0, respectively. The measure chosen to characterize the solutions is the sum of the horizontal and vertical velocities along the centreline at $(\psi, \phi) = (0, 1/4)$. The thin horizontal dotted lines are $u(0, 1/4) + v(0, 1/4) = 0$. Noting that $u(0, 1/4) = 0$ for the symmetric even-cell flows, these figures clearly show that the primary two-cell flows have upwelling along the centreline, while the disconnected two-cell flows have down-welling along the centreline. The symmetry-breaking bifurcation at the larger Marangoni number along the primary branch is supercritical in Fig. 3 since the aspect ratio 1.6 is less than that at the quartic bifurcation point, Q, Fig. 2a. The corresponding bifurcation point in Fig. 4 is subcritical since the aspect ratio 1.7 is greater than that at the quartic bifurcation point. Figures 3 and 4 both show branches of one-cell flows arising at symmetry-breaking bifurcation points terminating on the branch of two-cell flows with upwelling at the centre. This is consistent with the findings of Dijkstra [12] for horizontal free surfaces. Dijkstra argues that although initially purely antisymmetric, nonlinear effects cause clockwise rotating single-cell flows to become centred

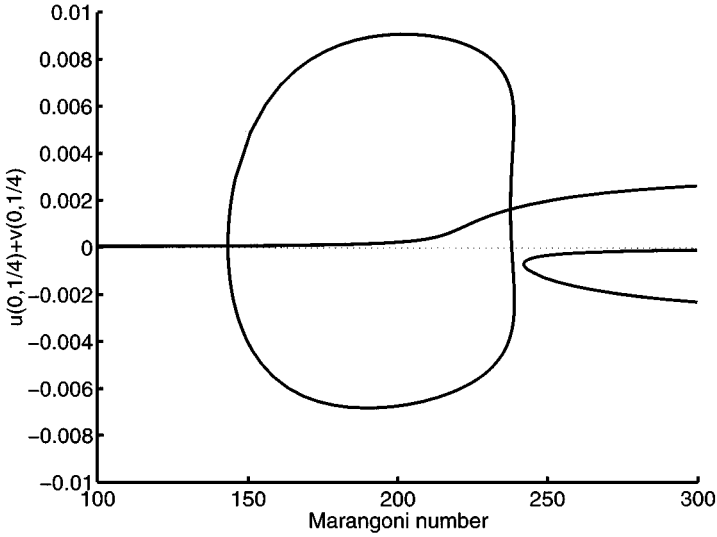

FIG. 3. Bifurcation diagram for $\eta = 1.6$, $\theta = 89.43$ degrees, and $Ca = 10^{-5}$. The ordinate is $u(0, 1/4) + v(0, 1/4)$.

nearer to the right hand wall, allowing a small anticlockwise rotating eddy to develop in the top left-hand corner. This eddy grows with Marangoni number and eventually a symmetric two-cell flow with upwelling at the centre arises. The same argument suitably modified applies to anticlockwise rotating cells. The two-cell flow arises either continuously (see [12], Fig. 4a) or via a hysteretic jump (see [12], Fig. 12b) according to whether the aspect ratio is greater than or less than that at the quartic point for 90 degree contact angles shown in Fig. 2a.

The loop of one-cell flows collapses at the $C+$ coalescence point C shown in Fig. 2, and for a range of aspect ratios exceeding that at this coalescence point, the bifurcation

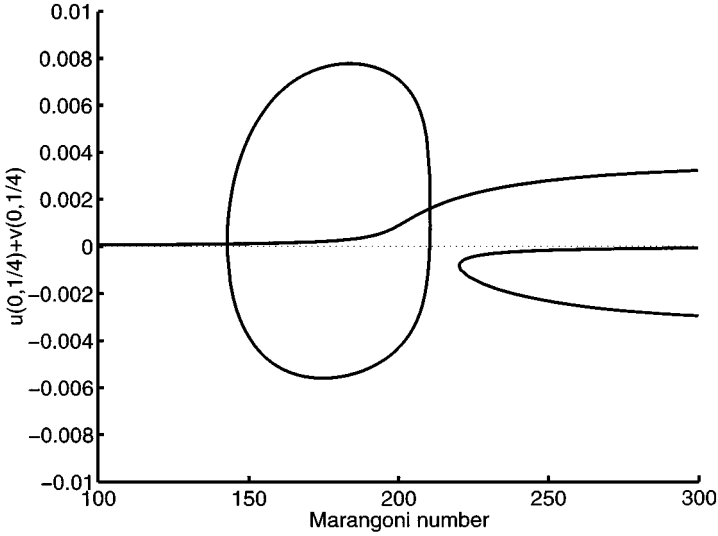

FIG. 4. Bifurcation diagram for $\eta = 1.7$, $\theta = 89.43$ degrees, and $Ca = 10^{-5}$. The ordinate is $u(0, 1/4) + v(0, 1/4)$.

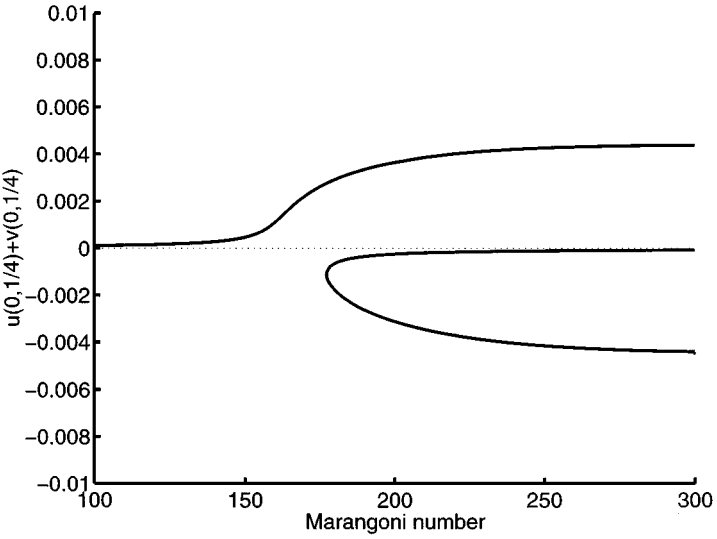

FIG. 5. Bifurcation diagram for $\eta = 2.0$, $\theta = 89.43$ degrees, and $Ca = 10^{-5}$. The ordinate is $u(0, 1/4) + v(0, 1/4)$.

diagrams are as shown in Fig. 5. As the contact angle decreases, the coalescence point moves rapidly towards smaller values of the aspect ratio and larger values of the Marangoni number, greatly reducing the region of parameter space in which one-cell flows can occur. In Fig. 6 we plot the critical Marangoni numbers for bifurcation to 1-cell and 2-cell flows for contact angles of 90 degrees, and the branch of symmetry-breaking bifurcation points

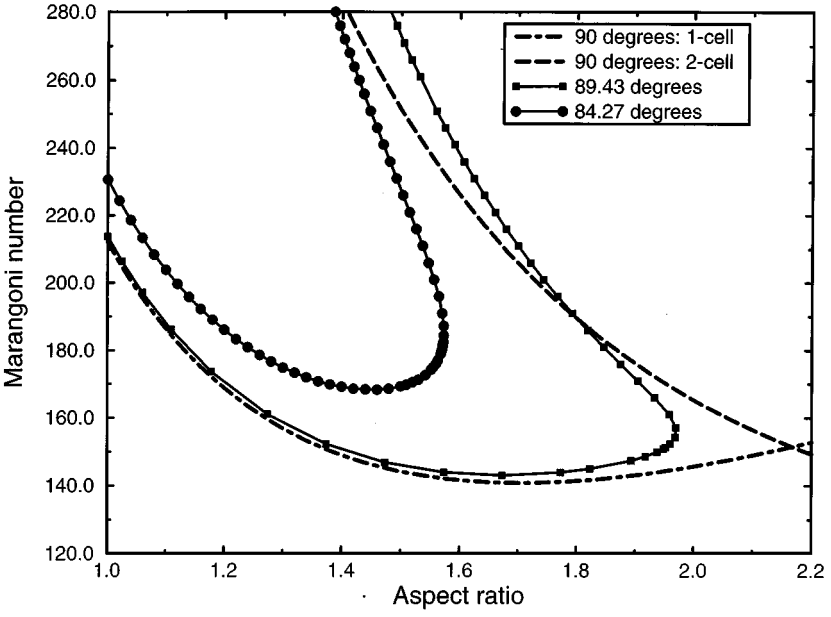

FIG. 6. Loci of singular points for $Ca = 10^{-5}$. The chained line is the locus of symmetry-breaking bifurcation points for a horizontal free surface. The dashed line is the locus of transcritical bifurcation points for a horizontal free surface. The two solid lines show the loci of symmetry-breaking bifurcation points on the primary two-cell branch for $\theta = 89.43$ degrees (squares) and 84.27 degrees (circles).

on the primary two-cell branch for contact angles of 89.43 and 84.27 degrees. It is clear that even contact angles close to 90 degrees disconnect the bifurcation structure by a large amount and comparisons between the horizontal rigid and deformable free-surface cases can only be sensibly made for contact angles near 90 degrees.

The symmetry breaking and symmetry preserving properties of the different types of singularities are evident from the null eigenvectors shown in Figs. 7a–e and 8a–e. The null eigenvector at the symmetry-breaking bifurcation point for aspect ratio 1.7 and Marangoni number 143 is shown in Fig. 7, and is clearly antisymmetric. The null eigenvector at the limit point of the disconnected two-cell flows at aspect ratio 1.7 and Marangoni number 221 is shown in Fig. 8, and is clearly symmetric. The null eigenvectors are scaled so that the v-component of the eigenvector at $(\psi, \phi) = (-1/4, 1/4)$ is equal to 1 in Fig. 7 and the v-component of the eigenvector at $(\psi, \phi) = (0, 1/8)$ is equal to 1 in Fig. 8.

The results of a convergence study for three of the more interesting singularities at contact angle of 89.4 degrees and capillary number of 10^{-5} are presented in Table 3. We have chosen to examine the convergence at the symmetry-breaking bifurcation point on the primary flow at the larger Marangoni number Ma_{B2}, and the limit point on the branch of one-cell flows at an aspect ratio of 1.6, Ma_{L2}. The limit point along the branch of disconnected two-cell flows at an aspect ratio of 1.7, Ma_{L1}, is also investigated. (Note that the symmetry-breaking bifurcation points were computed on Ω'_- using only one-half the number of elements indicated.)

In all three columns of Table 3, the critical Marangoni number appears to be converging with h at a rate that is faster than the linear rate expected on the basis of our test problems. However, the minimum free surface height (which occurs at $\psi = 0$) at the symmetry-breaking bifurcation points Ma_{B2}, converges at a rate that is more obviously linear, as is shown in Table 4.

Figures 9, 10, and 11 show the streamfunction and isotherms for the stable solutions at aspect ratio 1.7 and Marangoni numbers 100, 190, and 250, respectively.

The details of the mechanism by which one-cell and two-cell flows exchange stability as the aspect ratio increases when the free surface is constrained to be flat have been reported by Dijkstra [12]. An entirely analogous sequence of bifurcation diagrams arises when the free surface is deformed, differing only due to the disconnection of the transcritical bifurcations. When such comparisons are drawn, the disappearance of one-cell flows at the coalescence point C is not surprising, as it can be seen to correspond to the disappearance of the one-cell branches at the multiple bifurcation point when the free surface is horizontal and rigid. A further path of limit points and a path of Hopf bifurcation points have been omitted from Fig. 2b as a detailed comparison of the two exchange scenarios will appear later.

An interesting analytical result has been reported by Anderson and Davis [30]. These authors seek separable solutions to the coupled thermal and convection problem in wedge geometries with an insulating wall and an insulating free surface. For a contact angle $\theta = 90$ degrees, they find a separable solution which satisfies all but the normal stress boundary conditions, in which the temperature field has a logarithmic singularity at the corner. Their solution is valid in a neighbourhood of radius $r \ll d/Ma$ of the contact point between the insulated sidewall and the free surface. For contact angles $\theta < 90$ degrees, they present separable solutions, which again satisfy all but the normal stress boundary condition, in which the temperature and velocity fields are smooth and bounded. We have not observed any evidence of logarithmic behaviour in the temperature field for contact angles of 90 degrees. Anderson and Davis do not claim to have found the *only* possible solution and further note that, "This example shows that single-phase models with separable solutions forms may be too idealized in certain areas."

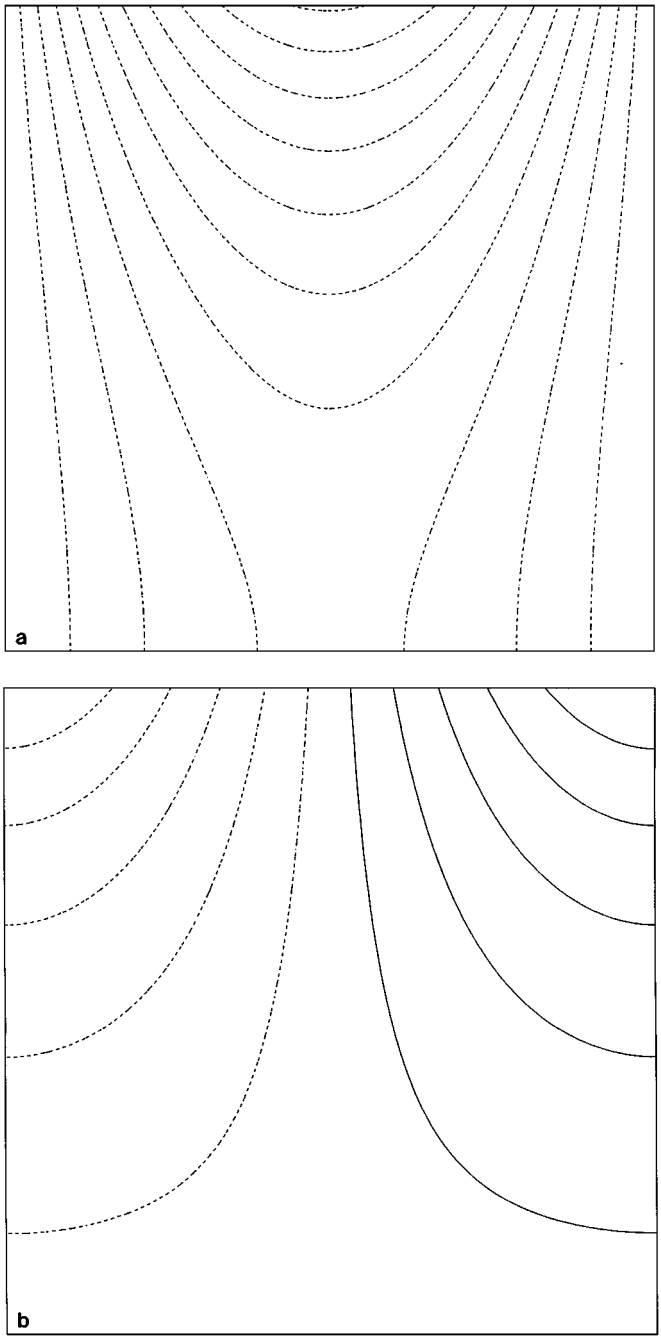

FIG. 7. Symmetry-breaking null eigenvector for $\eta = 1.7$, $Ma = 143.11$, $\theta = 89.43$ degrees, and $Ca = 10^{-5}$. Dashed lines correspond to negative values and solid lines to positive values. All contours are equally spaced. (a) x-component: contour values 0.0 to -1.25×10^{-2}; (b) y-component: contour values -1.8×10^{-2} to 1.8×10^{-2}; (c) u-component: contour values -3.5 to 16.5; (d) v-component: contour values -3.15 to 3.15; (e) T-component: contour values -45.0 to 45.0. The eigenvector is scaled so that the v-component at $(\psi, \phi) = (-1/4, 1/4)$ is equal to 1.

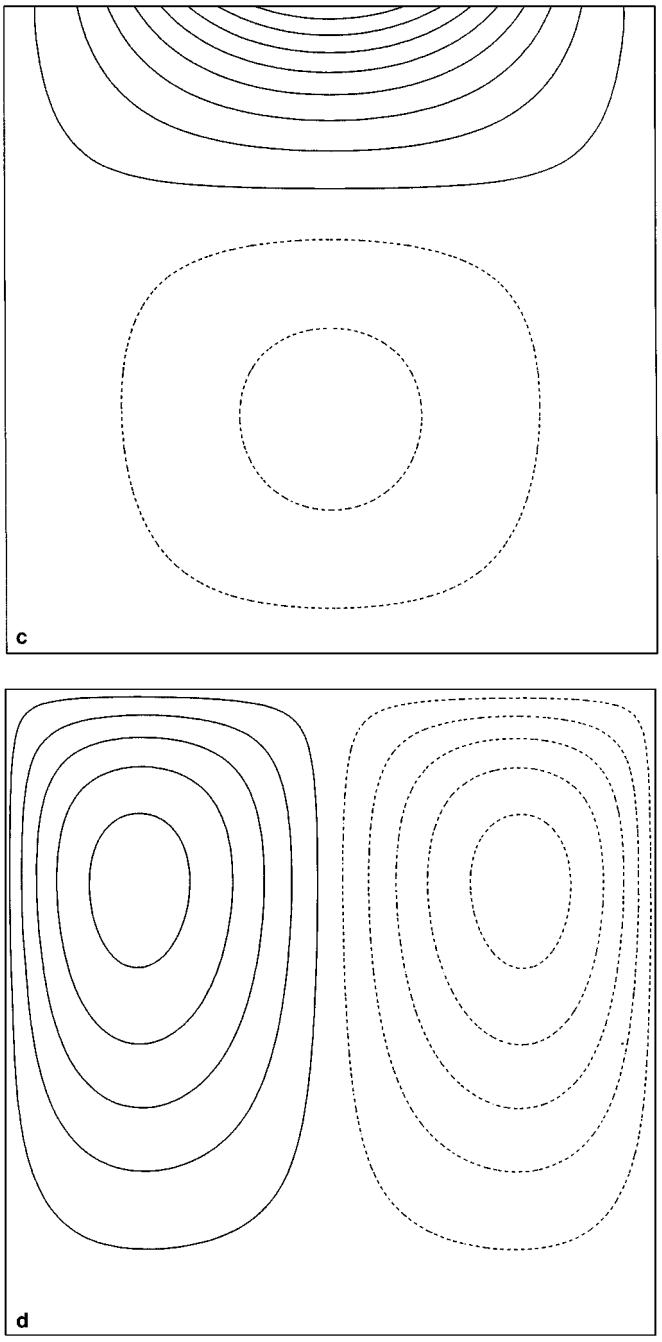

FIG. 7—*Continued*

In Table 5 we list the critical Marangoni numbers at limit points on two different convecting solution branches as a function of the contact angle θ. The limit point at Ma_{L1} occurs on the disconnected branch of two-cell flows at aspect ratio 1.6, and the limit point Ma_{L2} occurs on the single-cell flow branches an aspect ratio of 1.4. Both were computed for a capillary number of 10^{-5}. For contact angles $\theta < 90$ degrees, solutions with non-singular

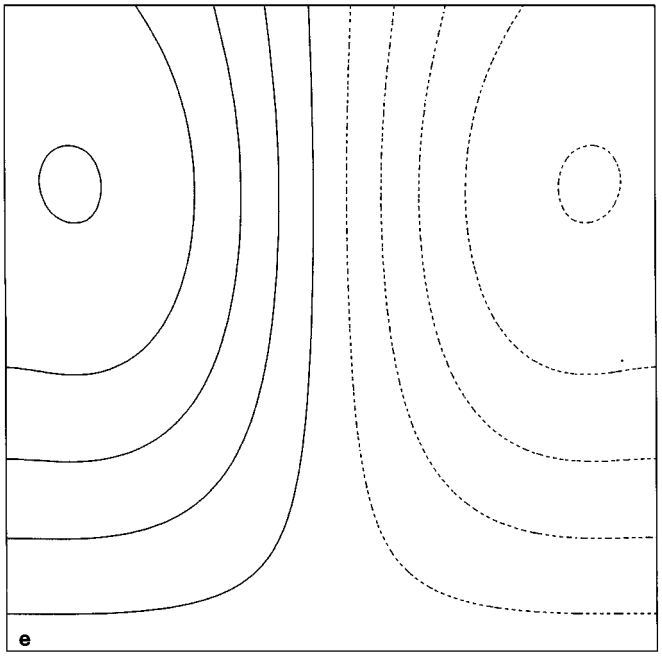

FIG. 7—*Continued*

temperature and velocity fields are presented by Anderson and Davis. As the contact angle increases, both critical Marangoni numbers converge smoothly to the value that is computed for a 90 degree contact angle. From the evidence presented in Table 5, it seems reasonable to suppose that we can accurately compute bifurcations from convecting flows even at contact angles of 90 degrees.

Our technique can of course be applied to flows with much larger free surface deformations as is indicated by the solutions shown in Figs. 12 and 13. Figure 12 illustrates a one-cell flow at an aspect ratio of 1.2 and a Marangoni number of 200, with a contact angle of 75.5 degrees and a capillary number of 2.75×10^{-3}. Keeping all other parameters fixed, single cell flows do not exist for much smaller contact angles than shown here.

Figure 13 illustrates a two-cell flow at an aspect ratio of 1.7 and a Marangoni number of 250, with a contact angle of 77.5 degrees and a capillary number of 2.75×10^{-3}. It is clear that much larger free surface deformations are possible for two-cell flows.

The temperature field for the conducting solution that exists for a 90 degree contact angle is linear with the isotherms parallel to the free surface, and is clearly regular at the contact point. This is not a contradiction of Anderson and Davis' result, since they found a singular temperature field at a contact angle of 90 degrees to be necessary only for their particular *separable, convecting* solutions. In Fig. 14 we plot the critical Marangoni number at the first symmetry-breaking bifurcation point against contact angle for an aspect ratio of one. We again observe very smooth behviour with respect to the contact angle. The limiting case at a contact angle of 90 degrees is the critical Marangoni number at the first symmetry-breaking bifurcation from the conducting solution. Moffatt [31] presents solutions for the externally driven isothermal flow near a sharp corner, in which one side of the wedge is a wall along which non-slip boundary conditions are applied and the other is a free surface. He shows that for contact angles less than approximately 78 degrees the solution is a series

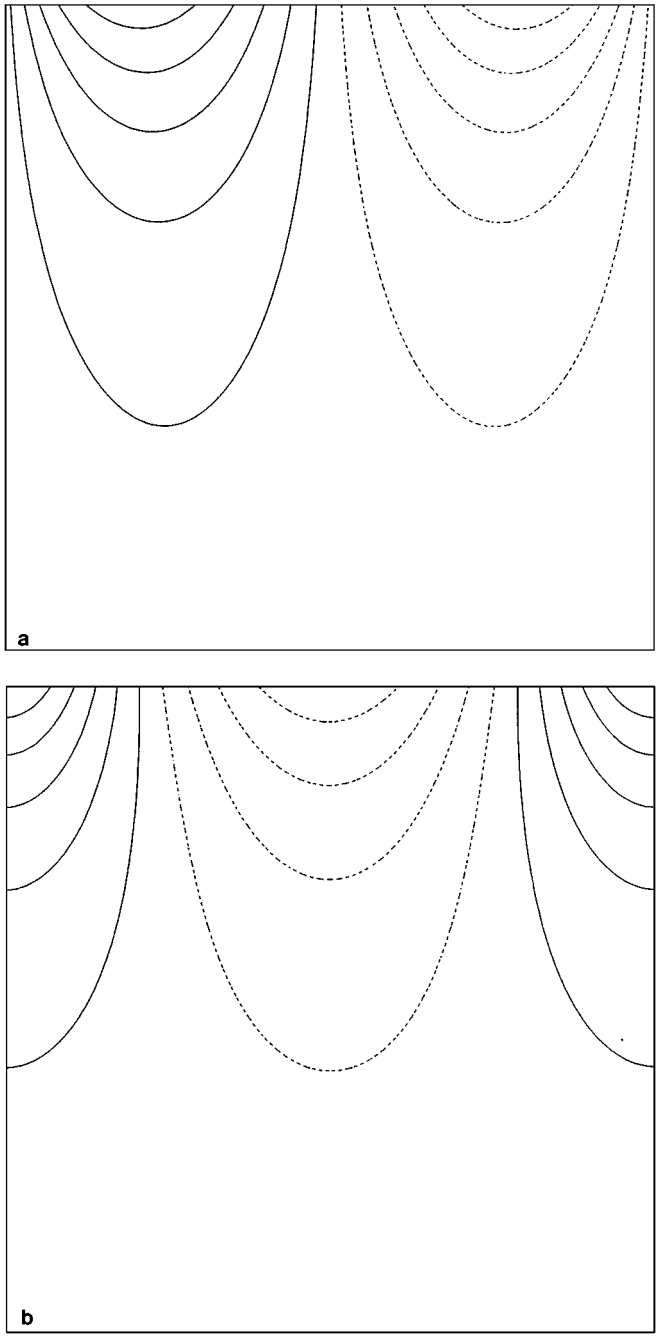

FIG. 8. Symmetry-preserving null eigenvector for $\eta = 1.7$, $Ma = 220.71$, $\theta = 89.43$ degrees, and $Ca = 10^{-5}$. Dashed lines correspond to negative values and solid lines to positive values. All contours are equally spaced. (a) x-component: contour values -9.0×10^{-3} to 9.0×10^{-3}; (b) y-component: contour values -1.6875×10^{-2} to 1.6875×10^{-2}; (c) u-component: contour values -45.0 to 45.0; (d) v-component: contour values -12.25 to 19.25; (e) T-component: contour values -124.875 to 124.875. The eigenvector is scaled so that the v-component at $(\psi, \phi) = (0, 1/8)$ is equal to 1.

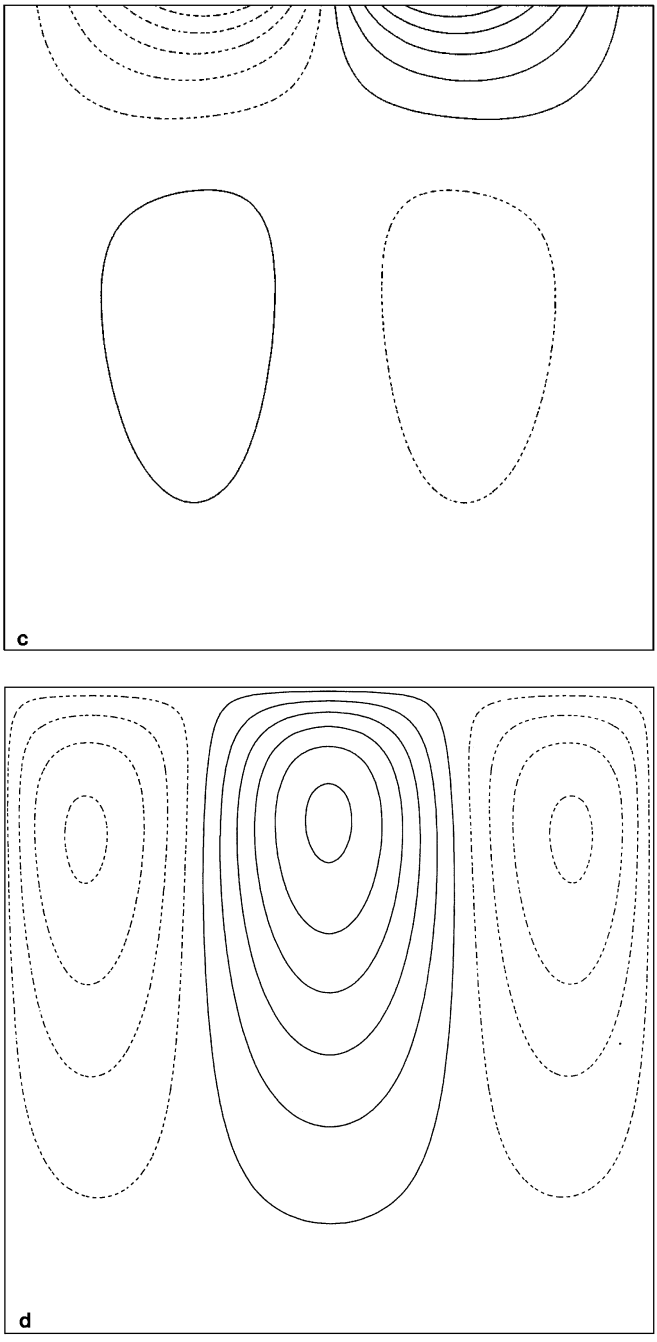

FIG. 8—*Continued*

of rapidly decaying eddies. We have not observed such eddies, and given their very rapid rate of decay, an extremely sensitive calculation would be required in order to observe them. We plan to conduct a more detailed investigation of corner flows with boundary conditions more closely approximating those of Anderson and Davis and Moffatt.

The power of extended system techniques to investigate a multi-dimensional parameter space is further illustrated in Fig. 15. We plot the critical Marangoni number at the first

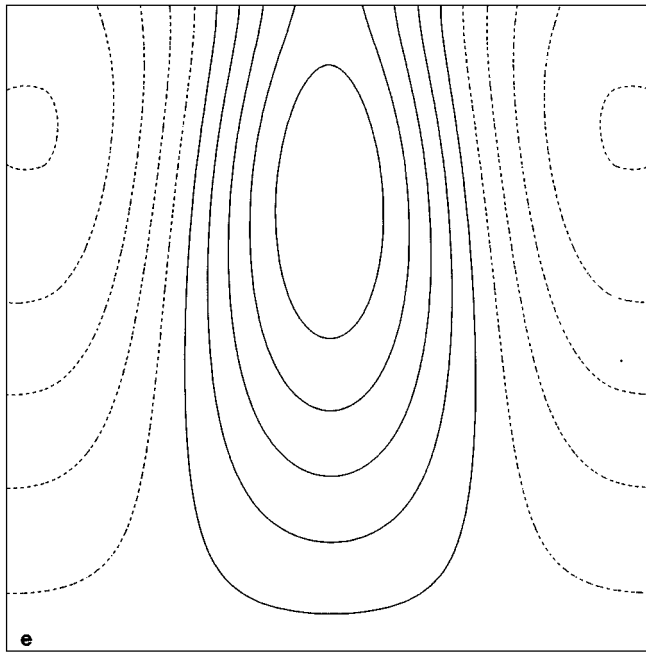

FIG. 8—*Continued*

symmetry-breaking bifurcation point at an aspect ratio of one, as the capillary number is varied between 0.1 and 10^{-5}.

6. CONCLUSIONS

We have developed a method for computing bifurcations of free-surface flows by combining an orthogonal mapping technique with an extended system approach for locating singularities. The mapping from the physical domain to a reference domain is computed as the solution to two coupled elliptic partial differential equations. First- and higher order derivatives of the discretized mapping equations, equilibrium equations, and nonlinear boundary conditions are required in order to construct and solve the extended systems by Newton's method. A computer algebra system, in our case REDUCE, was found to be essential to construct the subroutines to evaluate such derivatives. In two-dimensional domains, we have shown that contact angles other than 90 degrees produce the expected qualitative change (disconnection) in the bifurcations leading to Marangoni convection. Preliminary investigations have illustrated the power of our method to explore the multi-dimensional parameter space.

TABLE 3
Grid Refinement Study for the Location of Critical Points

Mesh	Ma_{L1}	Ma_{B2}	Ma_{L2}
16×16	220.712	238.069	239.282
32×32	220.661	238.033	239.244
64×64	220.656	238.031	239.242

TABLE 4
Grid Refinement Study for the Minimum Free Surface Height at a Critical Point

Mesh	Minimum free surface height
16×16	0.998653661
32×32	0.998653447
64×64	0.998653392

APPENDIX A: WEAK FORMULATION

The governing equations and boundary conditions can now be written in weak form in the usual manner. We make extensive use of Green's second identity

$$\int_\Omega g[\nabla \cdot \boldsymbol{F}]\, dA = \int_\Gamma g[\boldsymbol{n} \cdot \boldsymbol{F}]\, ds - \int_\Omega [\nabla g \cdot \boldsymbol{F}]\, dA$$

and transform integrals over the physical domain Ω to integrals over the reference domain Ω' where necessary.

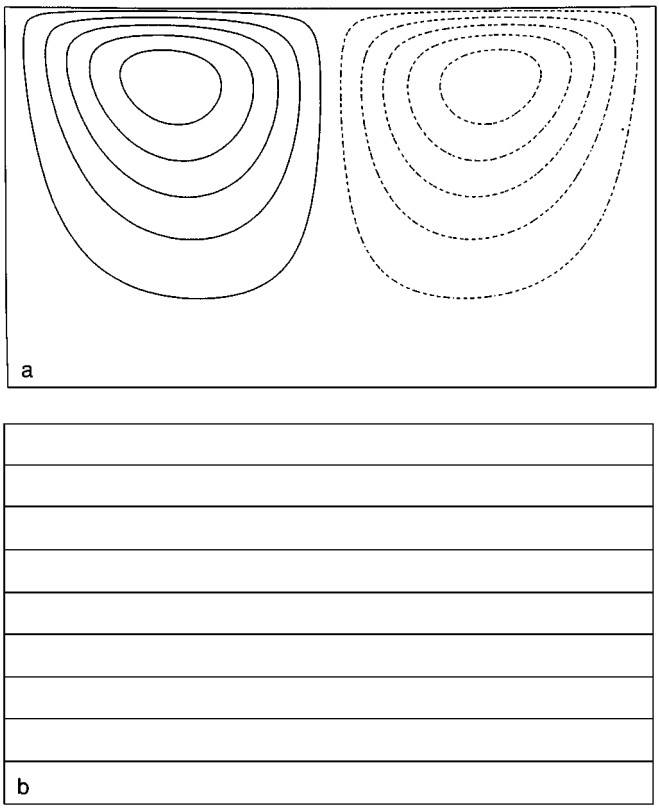

FIG. 9. Solution for $\eta = 1.7$, $Ma = 100$, $\theta = 89.43$ degrees, and $Ca = 10^{-5}$. (a) Streamfunction: contours are equally spaced between -5.4×10^{-5} and 5.4×10^{-5}. Dashed lines correspond to negative values (clockwise rotation) and solid lines to positive values (anticlockwise rotation). (b) Temperature: isotherms are equally spaced.

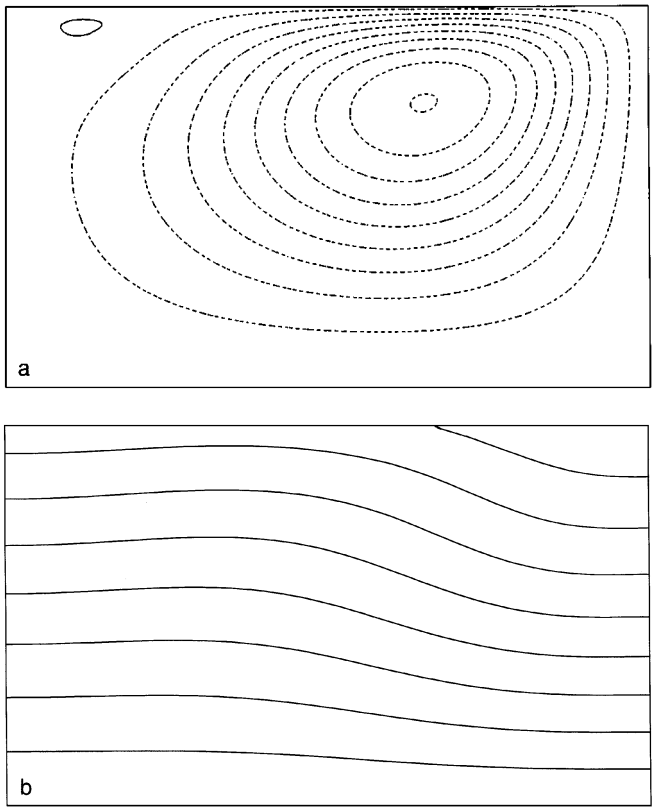

FIG. 10. Solution for $\eta = 1.7$, $Ma = 190$, $\theta = 89.43$ degrees, and $Ca = 10^{-5}$. (a) Streamfunction: contours are equally spaced between -3.4×10^{-3} and -2.0×10^{-4}. Dashed lines correspond to negative values (clockwise rotation). The solid line corresponds to 5.0×10^{-5} (anticlockwise rotation). (b) Temperature: isotherms are equally spaced.

Let $\xi^x(\psi, \phi)$ be a suitable test function. Then from (11) the weak equation for $x(\psi, \phi)$ is

$$\int_{\Omega'} \xi^x \left[(\lambda x_\psi)_\psi + \left(\lambda^{-1} x_\phi\right)_\phi \right] d\psi \, d\phi.$$

Rewriting this in divergence form

$$\begin{aligned}
&\int_{\Omega'} \xi^x \left[\nabla_{\prime} \cdot \begin{pmatrix} \lambda x_\psi \\ \lambda^{-1} x_\phi \end{pmatrix} \right] d\psi \, d\phi \\
&= \int_{\Gamma'} \xi^x \left[\boldsymbol{n}' \cdot \begin{pmatrix} \lambda x_\psi \\ \lambda^{-1} x_\phi \end{pmatrix} \right] ds - \int_{\Omega'} \left[\begin{pmatrix} \xi^x_\psi \\ \xi^x_\phi \end{pmatrix} \cdot \begin{pmatrix} \lambda x_\psi \\ \lambda^{-1} x_\phi \end{pmatrix} \right] d\psi \, d\phi \\
&= -\int_{\phi=1} y_\psi \xi^x \, d\psi - \int_{\Omega'} \left[(\lambda x_\psi) \xi^x_\psi + \left(\lambda^{-1} x_\phi\right) \xi^x_\phi \right] d\psi \, d\phi \\
&= 0, \qquad (21)
\end{aligned}$$

since test functions for $x(\psi, \phi)$ must be zero on $\psi = -1/2$ and $\psi = 1/2$ where Dirichlet boundary conditions are imposed, $x_\phi = 0$ on $\phi = 0$ and $\lambda^{-1} x_\phi = -y_\psi$ on $\phi = 1$.

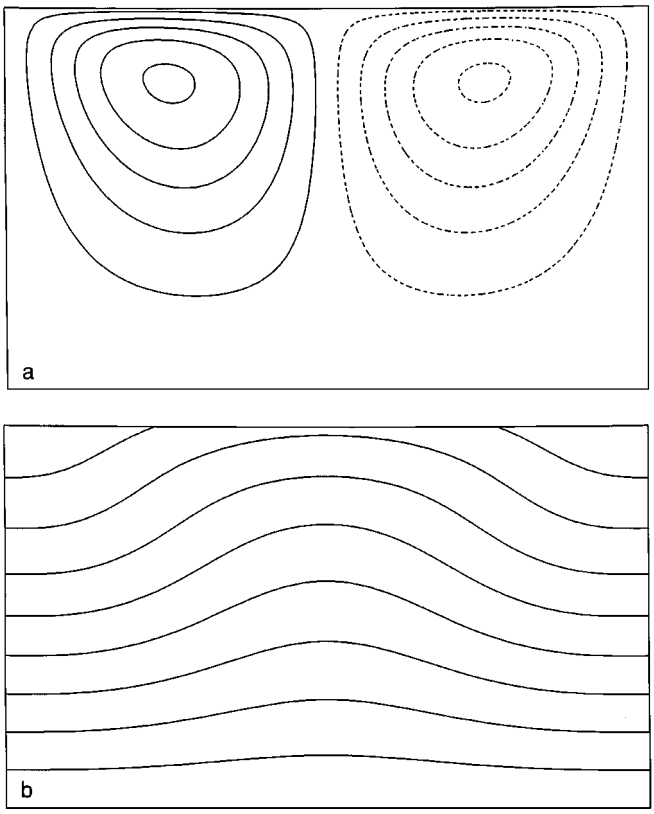

FIG. 11. Solution for $\eta = 1.7$, $Ma = 250$, $\theta = 89.43$ degrees, and $Ca = 10^{-5}$. (a) Streamfunction: contours are equally spaced between -2.7×10^{-3} and 2.7×10^{-3}. Dashed lines correspond to negative values (clockwise rotation) and solid lines to positive values (anticlockwise rotation). (b) Temperature: isotherms are equally spaced.

Similarly given a suitable test function $\xi^y(\psi, \phi)$, then from (12) the weak equation for $y(\psi, \phi)$ is

$$\begin{aligned}
&\int_{\Omega'} \xi^y \left[(\lambda y_\psi)_\psi + \left(\lambda^{-1} y_\phi\right)_\phi \right] d\psi\, d\phi \\
&= \int_{\Omega'} \xi^y \left[\nabla_{'} \cdot \begin{pmatrix} \lambda y_\psi \\ \lambda^{-1} y_\phi \end{pmatrix} \right] d\psi\, d\phi \\
&= \int_{\Gamma'} \xi^y \left[\boldsymbol{n}' \cdot \begin{pmatrix} \lambda y_\psi \\ \lambda^{-1} y_\phi \end{pmatrix} \right] ds - \int_{\Omega'} \left[\begin{pmatrix} \xi^y_\psi \\ \xi^y_\phi \end{pmatrix} \cdot \begin{pmatrix} \lambda y_\psi \\ \lambda^{-1} y_\phi \end{pmatrix} \right] d\psi\, d\phi \\
&= \int_{\phi=1} \lambda^{-1} y_\phi \xi^y\, d\psi - \int_{\Omega'} \left[(\lambda y_\psi) \xi^y_\psi + \left(\lambda^{-1} y_\phi\right) \xi^y_\phi \right] d\psi\, d\phi \\
&= 0, \qquad (22)
\end{aligned}$$

since test functions for $y(\psi, \phi)$ must be zero on $\phi = 0$ where a Dirichlet boundary condition is imposed and $y_\psi = 0$ on $\psi = -1/2$ and $\psi = 1/2$. The orthogonality condition along $\phi = 1$

TABLE 5
Critical Marangoni Numbers vs Contact Angle at Two Limit Points

Contact angle (radians)	Ma_{L1}	Ma_{L2}
$\pi/2 - 0.0100$	239.24	340.44
$\pi/2 - 0.0050$	242.17	346.54
$\pi/2 - 0.0010$	244.67	351.72
$\pi/2 - 0.0001$	245.25	352.92
$\pi/2$	245.32	353.06

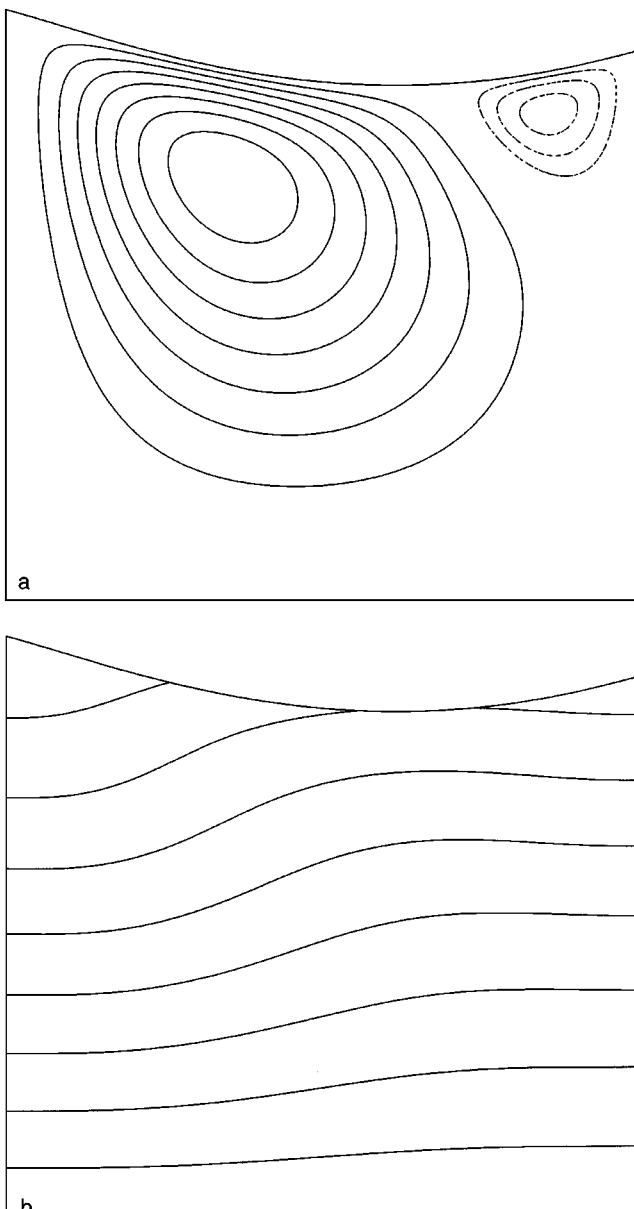

FIG. 12. Solution for $\eta = 1.2, Ma = 200, \theta = 75.5$ degrees, and $Ca = 2.75 \times 10^{-3}$. (a) Streamfunction: contours are -3.0×10^{-4}, -2.0×10^{-4}, -1.0×10^{-4}, then equally spaced between 4.5×10^{-4} and 3.15×10^{-3}. Dashed lines correspond to negative values (clockwise rotation) and solid lines to positive values (anticlockwise rotation). (b) Temperature: isotherms are equally spaced.

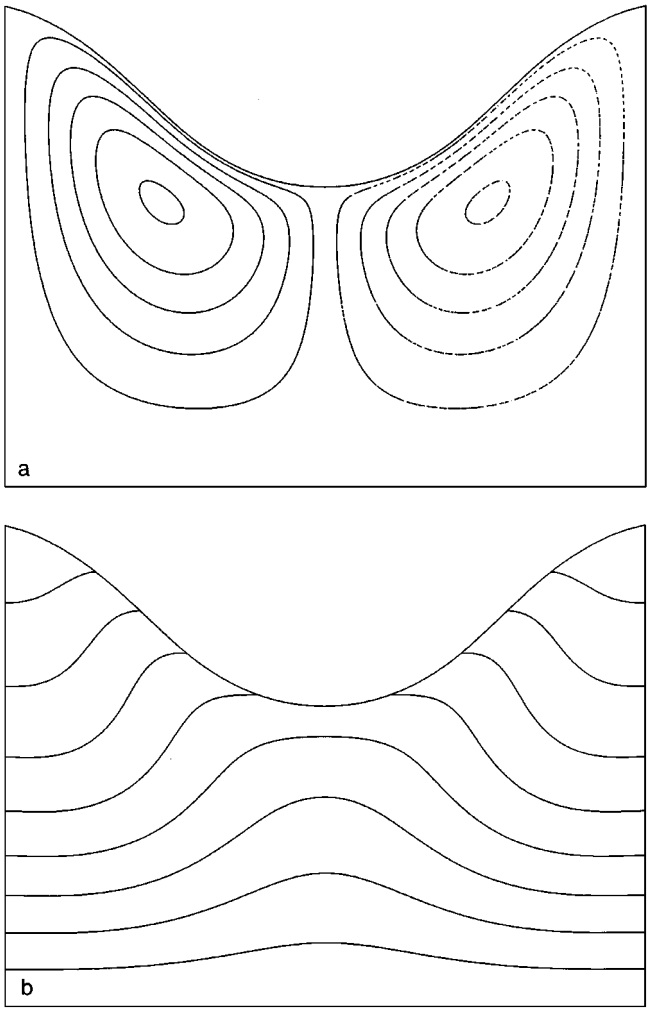

FIG. 13. Solution for $\eta = 1.7$, $Ma = 250$, $\theta = 77.5$ degrees, and $Ca = 2.75 \times 10^{-3}$. (a) Streamfunction: contours are equally spaced between -4.5×10^{-3} and 4.5×10^{-3}. Dashed lines correspond to negative values (clockwise rotation) and solid lines to positive values (anticlockwise rotation). (b) Temperature: isotherms are equally spaced.

is imposed via the x-equation. We use the discretized kinematic boundary to solve for the y-degree of freedom at a node along the free surface.

The weak equation for $\lambda(\psi, \phi)$ is

$$\begin{aligned}\int_{\Omega'} \xi^{\lambda}[\nabla_{\prime} \cdot \nabla_{\prime}\lambda]\, d\psi\, d\phi &= \int_{\Gamma'} \xi_{\lambda}[\boldsymbol{n}' \cdot \nabla_{\prime}\lambda]\, ds - \int_{\Omega'} [\nabla_{\prime}\xi^{\lambda} \cdot \nabla_{\prime}\lambda]\, d\psi\, d\phi \\ &= -\int_{\Omega'} \left[\lambda_{\psi}\xi^{\lambda}_{\psi} + \lambda_{\phi}\xi^{\lambda}_{\phi}\right] d\psi\, d\phi \\ &= 0, \end{aligned} \tag{23}$$

where $\xi^{\lambda}(\psi, \phi)$ is a suitable test function.

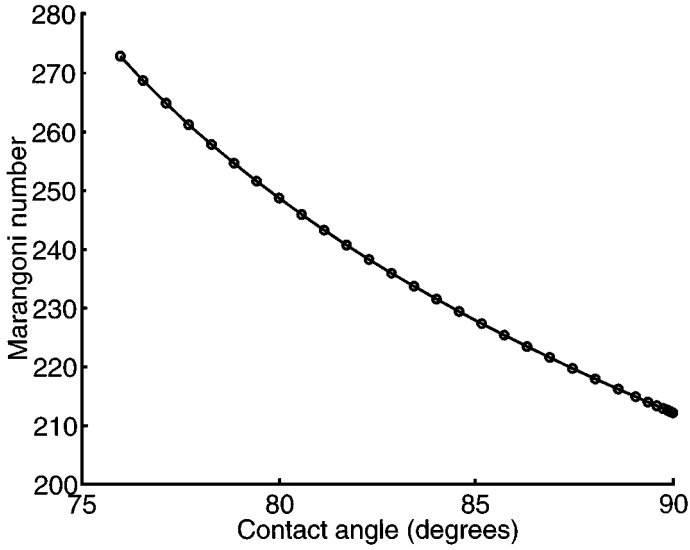

FIG. 14. Critical Marangoni number at the first symmetry breaking bifurcation point vs contact angle for $\eta = 1$ and $Ca = 10^{-5}$.

The weak form of the momentum equations is

$$\int_\Omega \xi^w \cdot \left[\frac{M}{Pr} \frac{D\boldsymbol{u}}{Dt} - \nabla \cdot \tau + \left(\frac{G}{MC} - \frac{RT}{M} \right) \boldsymbol{j} \right] dx\, dy = 0,$$

where

$$\xi^w = \begin{pmatrix} \xi^u(x(\psi, \phi), y(\psi, \phi)) \\ \xi^v(x(\psi, \phi), y(\psi, \phi)) \end{pmatrix}$$

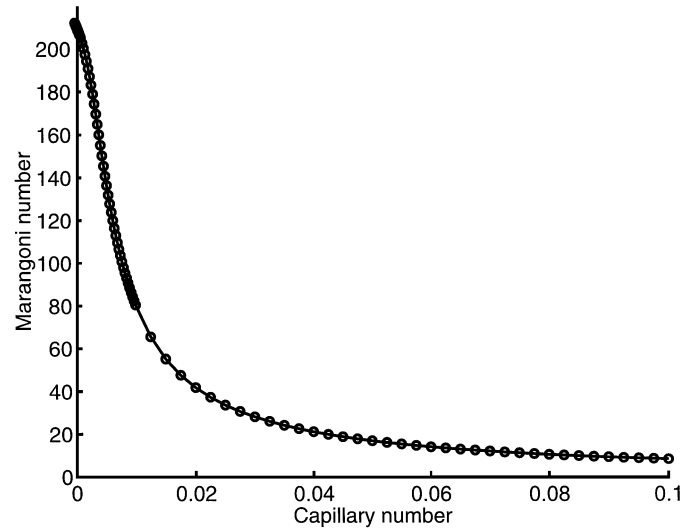

FIG. 15. Critical Marangoni number at the first symmetry breaking bifurcation point vs capillary number for $\eta = 1$ and $\theta = 90$ degrees.

is a suitable vector test function for the velocity

$$\begin{pmatrix} u(x(\psi,\phi), y(\psi,\phi)) \\ v(x(\psi,\phi), y(\psi,\phi)) \end{pmatrix}.$$

Derivatives with respect to x and y must be transformed to derivatives with respect to the independent variables ψ and ϕ, and the integral, which is initially taken over the physical domain Ω, must be transformed to an integral over Ω'.

The inertial terms are

$$\begin{aligned}
&\int_\Omega \xi^u \left[\frac{M}{Pr}\left(\frac{\partial u}{\partial t} + u\frac{\partial u}{\partial x} + v\frac{\partial u}{\partial y}\right)\right] dx\,dy \\
&\quad = \int_\Omega \xi^u \left[\frac{M}{Pr}\left(\frac{\partial u}{\partial t} + u(u_\psi \psi_x + u_\phi \phi_x) + v(u_\psi \psi_y + u_\phi \phi_y)\right)\right] dx\,dy \\
&\quad = \int_\Omega \xi^u \left[\frac{M}{Pr}\left(\frac{\partial u}{\partial t} + u(u_\psi y_\phi - u_\phi y_\psi)J^{-1} - v(u_\psi x_\phi - u_\phi x_\psi)J^{-1}\right)\right] dx\,dy \\
&\quad = \int_{\Omega'} \frac{M}{Pr}\left[J\frac{\partial u}{\partial t} + u(u_\psi y_\phi - u_\phi y_\psi) - v(u_\psi x_\phi - u_\phi x_\psi)\right]\xi^u\, d\psi\, d\phi, \qquad (24)
\end{aligned}$$

and

$$\begin{aligned}
&\int_\Omega \xi^v \left[\frac{M}{Pr}\left(\frac{\partial v}{\partial t} + u\frac{\partial v}{\partial x} + v\frac{\partial v}{\partial y}\right)\right] dx\,dy \\
&\quad = \int_{\Omega'} \frac{M}{Pr}\left[\boldsymbol{J}\frac{\partial v}{\partial t} + u(v_\psi y_\phi - v_\phi y_\psi) - v(v_\psi x_\phi - v_\phi x_\psi)\right]\xi^v\, d\psi\, d\phi. \qquad (25)
\end{aligned}$$

Applying Gauss's theorem

$$\int_\Omega \boldsymbol{F}_{j,j}\, dA = \int_\Gamma \boldsymbol{F}_j \boldsymbol{n}_j\, ds,$$

the term involving the divergence of the stress tensor becomes

$$\begin{aligned}
-\int_\Omega \xi_i^w \tau_{ij,j}\, dx\,dy &= -\int_\Gamma \xi_i^w \tau_{ij} n_j\, ds + \int_\Omega \xi_{i,j}^w \tau_{ij}\, dx\,dy \\
&= -\int_\Gamma \xi_i^w \tau_{ij} n_j\, ds + \int_\Omega \xi_{i,j}^w [-p\delta_{ij} + (u_{i,j} + u_{j,i})]\, dx\,dy. \qquad (26)
\end{aligned}$$

The pressure terms in (26) are

$$\begin{aligned}
-\int_\Omega p\frac{\partial \xi_i^w}{\partial x_i}\, dx\,dy &= -\int_\Omega p\left[\left(\xi_\psi^u \psi_x + \xi_\phi^u \phi_x\right) + \left(\xi_\psi^v \psi_y + \xi_\phi^v \phi_y\right)\right] dx\,dy \\
&= -\int_{\Omega'} p\left[\left(\xi_\psi^u y_\phi - \xi_\phi^u y_\psi\right) - \left(\xi_\psi^v x_\phi - \xi_\phi^v x_\psi\right)\right] d\psi\, d\phi. \qquad (27)
\end{aligned}$$

The first of the pair of velocity terms in (26) is

$$\begin{aligned}
&\int_\Omega u_{i,j}\xi^w_{i,j}\,dx\,dy \\
&\quad= \int_\Omega u_x\xi^u_x + u_y\xi^u_y + v_x\xi^v_x + v_y\xi^v_y\,dx\,dy \\
&\quad= \int_\Omega \big[(u_\psi\psi_x + u_\phi\phi_x)\big(\xi^u_\psi\psi_x + \xi^u_\phi\phi_x\big) + (u_\psi\psi_y + u_\phi\phi_y)\big(\xi^u_\psi\psi_y + \xi^u_\phi\phi_y\big) \\
&\qquad + (v_\psi\psi_x + v_\phi\phi_x)\big(\xi^v_\psi\psi_x + \xi^v_\phi\phi_x\big) + (v_\psi\psi_y + v_\phi\phi_y)\big(\xi^v_\psi\psi_y + \xi^v_\phi\phi_y\big)\big]\,dx\,dy \\
&\quad= \int_\Omega \big[u_\psi\big(\psi_x^2 + \psi_y^2\big)\xi^u_\psi + u_\phi(\psi_x\phi_x + \psi_y\phi_y)\xi^u_\psi + u_\psi(\psi_x\phi_x + \psi_y\phi_y)\xi^u_\phi \\
&\qquad + u_\phi\big(\phi_x^2 + \phi_y^2\big)\xi^u_\phi + v_\psi\big(\psi_x^2 + \psi_y^2\big)\xi^v_\psi + v_\phi(\psi_x\phi_x + \psi_y\phi_y)\xi^v_\psi \\
&\qquad + v_\phi(\psi_x\phi_x + \psi_y\phi_y)\xi^v_\psi + v_\phi\big(\phi_x^2 + \phi_y^2\big)\xi^v_\phi\big]\,dx\,dy \\
&\quad= \int_{\Omega'} \big[\lambda u_\psi\xi^u_\psi + \lambda^{-1}u_\phi\xi^u_\phi + \lambda v_\psi\xi^v_\psi + \lambda^{-1}v_\phi\xi^v_\phi\big]\,d\psi\,d\phi, \qquad (28)
\end{aligned}$$

since

$$\begin{aligned}
(\psi_x\phi_x + \psi_y\phi_y) &= \nabla\phi\cdot\nabla\psi \\
&= 0, \\
\psi_x^2 + \psi_y^2 &= \lambda\psi_x\phi_y - \lambda\psi_y\phi_x \\
&= \lambda[J^{-2}(y_\phi x_\psi - x_\phi y_\psi)] \\
&= \lambda J^{-1},
\end{aligned}$$

and

$$\begin{aligned}
\phi_x^2 + \phi_y^2 &= -\lambda^{-1}\phi_x\psi_y + \lambda^{-1}\phi_y\psi_x \\
&= -\lambda^{-1}[J^{-2}(y_\psi x_\phi - x_\psi y_\phi)] \\
&= \lambda^{-1}J^{-1}.
\end{aligned}$$

The second pair of velocity terms in (26) is

$$\begin{aligned}
&\int_\Omega u_{j,i}\xi^w_{i,j}\,dx\,dy \\
&\quad= \int_\Omega u_x\xi^u_x + v_x\xi^u_y + u_y\xi^v_x + v_y\xi^v_y\,dx\,dy \\
&\quad= \int_\Omega \big[(u_\psi\psi_x + u_\phi\phi_x)\big(\xi^u_\psi\psi_x + \xi^u_\phi\phi_x\big) + (v_\psi\psi_x + v_\phi\phi_x)\big(\xi^u_\psi\psi_y + \xi^u_\phi\phi_y\big) \\
&\qquad + (u_\psi\psi_y + u_\phi\phi_y)\big(\xi^v_\psi\psi_x + \xi^v_\phi\phi_x\big) + (v_\psi\psi_y + v_\phi\phi_y)\big(\xi^v_\psi\psi_y + \xi^v_\phi\phi_y\big)\big]\,dx\,dy. \qquad (29)
\end{aligned}$$

The coefficients of the test function derivatives are computed using REDUCE.

Along the free surface

$$\tau_{ij}n_j = \kappa\left(\frac{1}{MC} - T\right)\boldsymbol{n} - (\boldsymbol{t}\cdot\nabla T)\boldsymbol{t},$$

hence the boundary integral in (26) is

$$-\int_{\Gamma_F} \xi_i^w \left[\kappa\left(\frac{1}{MC} - T\right) n_i - (\boldsymbol{t}\cdot\nabla T) t_i\right] ds,$$

since the velocity test function is zero along Γ_L, Γ_R, and Γ_B where Dirichlet conditions are imposed. Using

$$\kappa n_i = \frac{dt_i}{ds}, \qquad \boldsymbol{t} = \frac{1}{\sqrt{x_\psi^2 + y_\psi^2}} \begin{pmatrix} x_\psi \\ y_\psi \end{pmatrix}, \qquad ds = \sqrt{x_\psi^2 + y_\psi^2}\, d\psi$$

along Γ_F, integrating by parts, and using the fact that the velocity test functions are zero at the left-hand and right-hand (LH and RH) ends of the free surface, we have

$$\begin{aligned}
&-\int_{\Gamma_F} \xi_i^w \left[\left(\frac{1}{MC} - T\right)\frac{dt_i}{ds} - (\boldsymbol{t}\cdot\nabla T) t_i\right] ds, \\
&\quad = -\left[\xi_i^w \left(\frac{1}{MC} - T\right) t_i\right]_{LH}^{RH} + \int_{\Gamma_F} \left[t_i \frac{d}{ds}\left(\xi_i^w \left(\frac{1}{MC} - T\right)\right) - \xi_i^w \frac{dT}{ds} t_i\right] ds, \\
&\quad = \int_{\Gamma_F} t_i \left(\frac{1}{MC} - T\right) \frac{d\xi_i^w}{ds}\, ds, \\
&\quad = \int_{\phi=1} \left(\frac{1}{MC} - T\right) \left(x_\psi \xi_\psi^u + y_\psi \xi_\psi^v\right) \frac{1}{\sqrt{x_\psi^2 + y_\psi^2}}\, d\psi. \qquad (30)
\end{aligned}$$

(Notice that the second term from the differentiation $\frac{d}{ds}(\xi_i(\frac{1}{MC} - T))$ cancels the term $\xi_i \frac{dT}{ds} t_i$ leading to the puzzling simplification.)

Finally, the weak form of the energy equation is

$$\int_\Omega \xi^T \left(M \frac{DT}{Dt} - \nabla^2 T\right) dx\, dy = 0,$$

where $\xi^T(x(\psi,\phi), y(\psi,\phi))$ is a suitable test function. The convection term is

$$\begin{aligned}
&\int_\Omega \xi^T \left(M \frac{DT}{Dt}\right) dx\, dy \\
&\quad = \int_\Omega \xi^T M \left(\frac{\partial T}{\partial t} + \boldsymbol{u}\cdot\nabla T\right) dx\, dy \\
&\quad = \int_\Omega \xi^T M \left(\frac{\partial T}{\partial t} + u\frac{\partial T}{\partial x} + v\frac{\partial T}{\partial y}\right) dx\, dy \\
&\quad = \int_\Omega \xi^T M \left[\frac{\partial T}{\partial t} + u(T_\psi \psi_x + T_\phi \phi_x) + v(T_\psi \psi_y + T_\phi \phi_y)\right] dx\, dy \\
&\quad = \int_\Omega \xi^T M \left[\frac{\partial T}{\partial t} + u(T_\psi y_\phi - T_\phi y_\psi) J^{-1} + v(T_\psi x_\phi - T_\phi x_\psi) J^{-1}\right] dx\, dy \\
&\quad = \int_{\Omega'} M \left[J\frac{\partial T}{\partial t} + u(T_\psi y_\phi - T_\phi y_\psi) + v(T_\psi x_\phi - T_\phi x_\psi)\right] \xi^T\, d\psi\, d\phi. \qquad (31)
\end{aligned}$$

The diffusive term is

$$-\int_\Omega \xi^T(\nabla\cdot\nabla T)\,dx\,dy = -\int_\Gamma \xi^T[\boldsymbol{n}\cdot\nabla T]\,ds + \int_\Omega [\nabla\xi^T\cdot\nabla T]\,dx\,dy. \tag{32}$$

The integral over Ω in (32) is

$$\begin{aligned}
&\int_\Omega \left[\frac{\partial T}{\partial x}\frac{\partial \xi^T}{\partial x} + \frac{\partial T}{\partial y}\frac{\partial \xi^T}{\partial y}\right] dx\,dy \\
&\quad= \int_\Omega \left[(T_\psi\psi_x + T_\phi\phi_x)\left(\xi^T_\psi\psi_x + \xi^T_\phi\phi_x\right) + (T_\psi\psi_y + T_\phi\phi_y)\left(\xi^T_\psi\psi_y + \xi^T_\phi\phi_y\right)\right] dx\,dy \\
&\quad= \int_\Omega [(T_\psi\psi_x + T_\phi\phi_x)\psi_x + (T_\psi\psi_y + T_\phi\phi_y)\psi_y]\xi^T_\psi \\
&\qquad + [(T_\psi\psi_x + T_\phi\phi_x)\phi_x + (T_\psi\psi_y + T_\phi\phi_y)\phi_y]\xi^T_\phi\,dx\,dy \\
&\quad= \int_\Omega \left[(T_\psi\left(\psi_x^2 + \psi_y^2\right) + T_\phi(\phi_x\psi_x + \phi_y\psi_y)\right]\xi^T_\psi \\
&\qquad + \left[T_\psi(\psi_x\phi_x + \psi_y\phi_y) + T_\phi\left(\phi_x^2 + \phi_y^2\right)\right]\xi^T_\phi\,dx\,dy \\
&\quad= \int_{\Omega'} \left[(\lambda T_\psi)\xi^T_\psi + (\lambda^{-1}T_\phi)\xi^T_\phi\right] d\psi\,d\phi.
\end{aligned} \tag{33}$$

The boundary integral in (32) is zero along Γ_L and Γ_R where $\boldsymbol{n}\cdot\nabla T = 0$ and along Γ_B where the temperature is imposed as a Dirichlet condition, hence the integral reduces to

$$\begin{aligned}
-\int_{\Gamma_F} \xi^T(\boldsymbol{n}\cdot\nabla T)\,ds &= \int_{\Gamma_F} \xi^T(LT)\,ds \\
&= \int_{\phi=1} \left(LT\sqrt{x_\psi^2 + y_\psi^2}\right)\xi^T\,d\psi.
\end{aligned} \tag{34}$$

ACKNOWLEDGMENTS

S. J. Tavener thanks the National Science Foundation for supporting this work under Grant DMS 94-03915, and thanks the Oxford University Computing Laboratory and Professor Tom Mullin of the University of Manchester for access to computing facilities. Both authors gratefully acknowledge the continuing support of A.E.A. Technology. We also thank D. M. Anderson and S. H. Davis for helpful discussions.

REFERENCES

1. J. R. A. Pearson, On convection cells induced by surface tension, *J. Fluid Mech.* **4**, 489 (1958).
2. S. H. Davis, Thermocapillary instabilities, *Ann. Rev. Fluid Mech.* **17**, 403 (1987).
3. K. A. Cliffe, S. J. Tavener, and A. A. Wheeler, An orthogonal mapping technique for the computation of a viscous free-surface flow, *Int. J. Numer. Methods Fluids* **15**, 1243 (1992).
4. G. Riskin and L. G. Leal, Orthogonal mapping, *J. Comput. Phys.* **50**, 71 (1983).
5. K. Tsiveriotis and R. A. Brown, Boundary-conforming mapping applied to computations of highly deformed solidification interfaces, *Int. J. Numer. Methods Fluids* **14**, 981 (1992).
6. K. N. Christadoulou and L. E. Scriven, Discretization of free surface flows and other moving boundary problems, *J. Comput. Phys.* **99**, 39 (1992).
7. K. A. Cliffe and A. Spence, The calculation of high order singularities in the Taylor problem, in *Numerical Methods for Bifurcation Problems*, edited by T. Kupper, H. D. Mittelmann, and H. Weber, Int. Ser. Numer. Math. (Birkäuser, Basel, 1984), Vol. 70, p. 129.

8. K. A. Cliffe, A. D. Jepson, and A. Spence, The numerical calculation of bifurcation problems with symmetry with application to the finite Taylor problem, in *Numerical Methods for Fluid Dynamics*, edited by K. W. Morton and M. J. Baines (Clarendon, Oxford, 1986), Vol. II, p. 155.
9. K. A. Cliffe and A. Spence, Numerical calculations of bifurcations in the finite Taylor problem, in *Numerical Methods for Fluid Dynamics*, edited by K. W. Morton and M. J. Baines (Clarendon, Oxford, 1986), Vol. II, p. 155.
10. A. C. Hearn, *REDUCE Users Manual* (Rand Publication CP78, 1987).
11. K. H. Winters, Th. Plesser, and K. A. Cliffe, The onset of convection in a finite container due to surface tension and buoyancy, *Phys. D* **29**, 387 (1988).
12. H. A. Dijkstra, On the structure of cellular solutions in Rayleigh–Bénard–Marangoni flows in small-aspect-ratio containers, *J. Fluid Mech.* **243**, 73 (1992).
13. A. Bergeon, D. Henry, and H. Ben Hadid, Marangoni–Bénard instability in microgravity conditions with Soret effect, *Int. J. Heat Mass Transfer* **37**, 1545 (1994).
14. E. Evrenselamet, V. S. Arapci, and A. T. Chai, Thermocapillary-driven flow past the Marangoni instability, *Numer. Heat Trans. A* **26**, 521 (1994).
15. A. A. Zaman and R. Narayanan, Interfacial and buoyancy-driven convection—The effect of geometry and comparison with experiment, *J. Colloid Inter. Sci.* **179**, 151 (1996).
16. H. A. Dijkstra, Surface-tension driven cellular-patterns in 3-dimensional boxes—Linear stability, *Microgravity Sci. Tech.* **7**, 307 (1995).
17. H. A. Dijkstra, Surface-tension driven cellular-patterns in 3-dimensional boxes. 2. A bifurcation study, *Microgravity Sci. Tech.* **8**, 70 (1995).
18. P. D. Dauby and G. Lebon, Marangoni–Bénard instability in rigid rectangular containers, *J. Fluid. Mech.* **329**, 25 (1996).
19. J. C. Chen, J. C. Sheu, and S. S. Jwu, Numerical computation of thermocapillary convection in a rectangular cavity, *Numer. Heat Trans.* **17**, 287 (1990).
20. J. M. Floryan and C. Chen, Thermocapillary convection and existence of continuous liquid layers in the absence of gravity, *J. Fluid Mech.* **277**, 303 (1994).
21. W. Q. Lu, Boundary-element analysis of thermocapillary convection with a free-surface in a rectangular cavity, *Int. J. Heat Mass Transfer* **37**, 1063 (1994).
22. G. P. Sasmal and J. I. Hochstein, Marangoni convection with a curved and deforming free-surface in a cavity, *J. Fluids Eng.* **116**, 577 (1994).
23. S. Chippada, T. C. Jue, and B. Ramaswamy, Finite-element simulation of combined buoyancy and thermocapillary driven convection in open cavities, *Int. J. Numer. Methods Eng.* **38**, 335 (1995).
24. Y. Kamotami, S. Ostrach, and A. Pline, Analysis of velocity data in surface tension driven convection experiment in microgravity, *Phys. Fluids* **6**, 3601 (1994).
25. Y. Kamotami and J. Platt, Effects of free surface shape on combined thermocapillary and natural convection, *J. Thermophys. Heat Transfer* **6**, 721 (1992).
26. B. Werner and A. Spence, The computation of symmetry-breaking bifurcation points, *SIAM J. Numer. Anal.* **21**, 388 (1984).
27. G. Moore and A. Spence, The calculation of turning points of nonlinear equations, *SIAM J. Numer. Anal.* **17**, 567 (1980).
28. V. Girault and P.-A. Raviart, *Finite Element Methods for Navier–Stokes Equations, Theory and Algorithms* (Springer-Verlag, New York, 1986).
29. S. C. Brenner and L. R. Scott, *The Mathematical Theory of Finite Element Methods* (Springer-Verlag, New York, 1994).
30. D. M. Anderson and S. H. Davis, Local fluid and heat flow near contact lines, *J. Fluid Mech.* **268**, 231 (1994).
31. H. K. Moffatt, Viscous and resistive eddies near a sharp corner, *J. Fluid Mech.* **18**, 1 (1964).